MSc Physics and Astronomy

Biophysics and Biophotonics

Master Thesis

Enhancing Passive Radiative Cooling for Solar Cells with Photonic Microstructures

---

by

Evelijn Akerboom

11323515

July 2021
60EC
September 2020 – July 2021

Daily supervisor:
Tom Veeken

Supervisor/Examiner: *Examiner:*
Prof. Dr. Albert Polman   Dr. Jorik van de Groep

AMOLF physics of functional complex matter

Abstract

Passive radiative cooling (PRC) can be applied to solar cells, using the spontaneous emission of infrared (IR) thermal radiation to dissipate heat into space continuously. The challenge is to enhance PRC while simultaneously keeping the structure transparent in the visible wavelength range. In this thesis, we propose two designs to optimize PRC: a close-packed monolayer of glass spheres as a coating for a bare silicon solar cell, and a hexagonal array of silica cylinders etched in the top surface for a silica-based solar module. FDTD simulations are used to optimize the geometry for maximum emissivity in the IR wavelength range. Next, the optimized structures are fabricated using drop-casting for the spherical coating, and UV-lithography in combination with reactive ion etching, for the patterning of silica. The emissivity of both samples is measured using Fourier Transform Infrared Spectroscopy (FTIR), extended with an integrating sphere, and the measurements compare well to the FDTD simulations. Both designs show a significant increase in emissivity in the IR without reducing the incoupling of visible light. Finally, we measure the temperature in time at the AMOLF rooftop under direct sunlight to determine the radiative cooling rate. A considerable variation was observed in identical samples, but both our structures showed a temperature reduction with respect to bare silicon. We have designed a PRC structure that can be applied to any solar cell, either with or without glass encapsulation, and PRC, in general, could improve all outdoor devices that benefit from a lower operating temperature.

Contents

1 Introduction

In recent years, a lot of effort has been put into improving and optimizing the power conversion efficiency of solar cells. From the detailed balance limit[1] we know the fundamental efficiency limit for every type of solar cell, which is 29.7% for silicon-based solar cells[2]. Due to recent advances in the development of silicon solar cells, a record efficiency is reached of 27.6%[3]. Efficiency measurements are done at constant conditions, i.e., illumination of 1 sun at an operating temperature of 25 ^{o}C. However, due to hot-carrier cooling and non-radiative recombination, a silicon solar cell can reach operating temperatures up to $60\ ^o$C under direct sunlight. These high temperatures reduce the solar conversion efficiency[4] and the lifetime of the cell[5].

Figure 1.1 shows a linear relation between η_T/η_{Tref} - the ratio of temperature-dependent efficiency to the efficiency at reference temperature – for silicon-based solar cells and the operating temperature. A relative efficiency drop is shown up to 0.45% for every 1K in temperature rise. Meaning that a silicon solar cell suffers a 15.75% relative efficiency drop at an operating temperature of 60 ^{o}C. Furthermore, the lifetime will halve for every 10 degrees in temperature rise [5]. Therefore, it is important to find a way to cool the module without extra energy input. One way to do this is by passive radiative cooling.
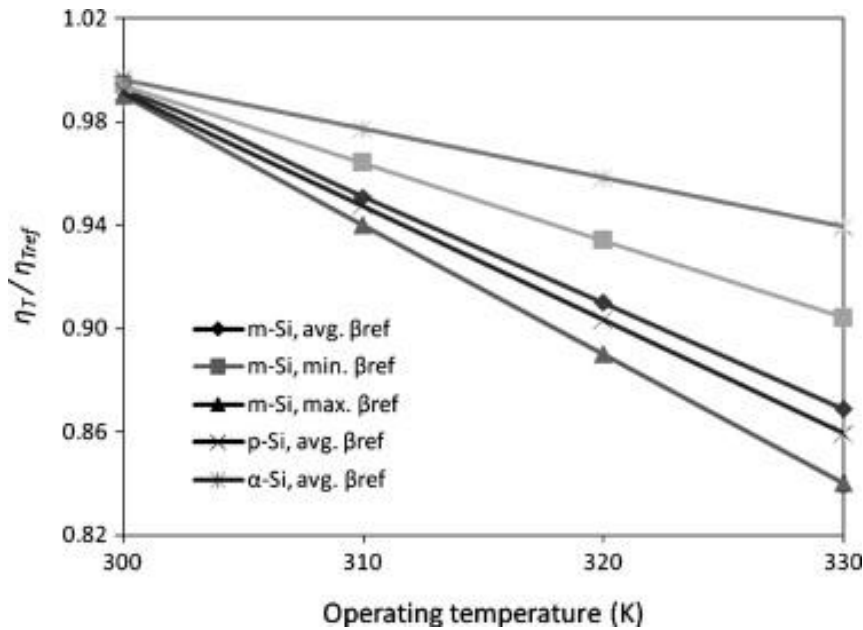

Figure 1.1: The calculated ratio of temperature-dependent efficiency to the efficiency at reference temperature ($\eta_T/\eta_{T_{ref}}$) versus operating temperature, for a silicon-based solar cell. [4]

The concept of passive radiative cooling (PRC) is to use the thermal emission of an object to dissipate heat continuously. According to the thermodynamic principle, two objects with different temperatures will exchange heat via thermal radiation until an equilibrium temperature is reached. The amount of heat emitted as thermal radiation scales with the temperature of an object, so effectively, heat is transferred from the warmer object to the colder object. Thus, to cool a warm object with thermal emission, a colder object is needed, which acts as the heat sink. The perfect heat sink is outer space due to the temperature of about 3 K and the immense volume. The concept of emitting thermal radiation into outer space is the core principle of PRC.

In the last decade, interest in PRC has grown in several applications, from dew collection in remote and dry places[6] to the cooling of buildings[7]. In 2014, Raman et al. showed a 4.9 sub-ambient cooling using a thin-film multilayer to optimize the radiative properties of the structure [8]. The multilayer was designed to enhance PRC while simultaneously exclude heating by reflecting all incident solar radiation. The high reflectance in the visible makes it unsuitable for the application for solar cells since a solar cell wants to absorb all light with higher energy than the bandgap.

Recently, the application of PRC for solar cells has gained interest, and it has been shown effective in several ways. First of all, numerous materials can be used and secondly different methods. The most prevalent techniques are multilayers [9,10], 2D structures [11–16], a combination of the two [17,18], or an effective medium [19–21].

Table 1.1 shows a complete outline of the recent advances in PRC for solar cells. To be able to compare different reported temperature reductions, it is essential to know what they use as a reference. Often, two temperature reductions are reported; one with respect to bare silicon and a second with respect to silicon covered with silica, to resemble a solar module (shown in the table as Si or Si+SiO2, respectively). In this thesis we will see a significant difference between the radiative cooling ability of a bare silicon solar cell and that of a silica-based solar cell.

Table 1.1: Advances of passive radiative cooling for solar cells in the last decade, with the used structure, the reference sample, and the showed temperature reduction with respect to the reference sample calculated, in italic, or measured, in bold.

First Author (year)	Structure	Reference sample	Temperature reduction (K)
Perrakis (2021) [11]	SiO_2 square micro grating with nanopillars on top	Si Si+ SiO_2	*5.8* *0.2*
Zhai (2021) [19]	PDMS layer with embedded SiO_2 nano-particles	PDMS	**2.1**
Chen (2021)[20]	TPX coating with embedded SiO_2 nano-particles	Si SC	*5*
Zahir (2021) [10]	Multilayer TiO_2/BK7	Si SC Si+ SiO_2	*18.4* *5.4*
Gao (2020) [17]	Multilayer of TiO_2/SiO_2 with a pyramid structure	Si SC	*15.6*
Ziming (2020) [21]	Polymer embedded with SiO_2 micro-particles	ambient	**8.7**
Fernandez (2019)[12]	Self-assembly of SiO_2 spheres	Si Si+SLG	**14** **9**
Long(2019) [13]	SiO_2 square lattice of micro-cylinders	Si	*20* **(2)**
Lee (2019) [14]	PDMS square lattice of pyramids	Si SC	*13*
Zhao (2018) [18]	Multilayer TiO_2/SiO_2 with square lattice of air cylinders	Si SC Si+ SiO_2	*12.0* *8.3*
Li (2017) [9]	Multilayer of Al_2O_3/SiN/TiO_2/SiN on SiO_2	Si solar module	*5.7*
Zhu (2015) [15]	Square lattice of air holes in SiO_2	Si Si+ SiO_2	**13** **1**
Zhu (2014) [16]	SiO_2 square lattice of pyramids	Si Si+ SiO_2	*17.6* *5.9*

Furthermore, the temperature reduction can be calculated (italic) – using simulated or measured optical spectra from the designed structure – or measured (bold) under direct sunlight. Most articles only report a theoretical temperature reduction based on measured optical properties of their structures, but only a few show a measured temperature reduction. The largest temperature reduction, both with respect to bare silicon and to silicon covered with silica, is demonstrated by Fernandez et al.[12] They measured an average temperature reduction of 14 and 9 degrees, respectively, using a self-assembled monolayer of silica spheres with a diameter of 8 μm.

1.1   Outline

In this thesis, we propose a coating of resonant microstructures for PRC for solar cells that enhances the cooling while keeping the structure transparent in the visible wavelength range. In Chapter 2, the general theory of PRC is discussed, concluding with a general condition for the best optical properties for the PRC enhancement for solar cells.

Subsequently, we will discuss several ways to tune the optical properties of a structure based on general light theory and Mie resonances in Chapter 3. We will see that the radiative properties of a bare silicon solar cell are poor and that by adding the module glass – often used to protect the solar cell – it is already significantly increased. Therefore, we propose and optimize two designs to enhance PRC: a coating of close-packed silica spheres for a bare silicon solar cell and a hexagonal array of silica cylinders etched into the surface of a silica-based solar module.

In Chapter 4, we discuss the fabrication of both designs. First, a silicon substrate is coated with gold from the back to exclude transmission, and this is used as a basis for both designs. Next, the coating of close-packed silica spheres is made bottom-up, using drop-casting on the silicon substrate. The cylinders are etched into a silica substrate and put on top of a silicon substrate using immersion oil as a refractive index matching fluid. With optical measurements, the improvement of the radiative properties is shown using our structures in Chapter 5, and the results compare well with the FDTD simulations in combination with TMM calculations.

Finally, we show a reduced measured temperature of the silicon substrate with a temperature measurement on the AMOLF rooftop under direct sunlight in Chapter 6, and we end with a brief summary of the main findings of this thesis and an outlook for future applications and improvements.

2   Passive radiative cooling

PRC is a continuous way of cooling that can be applied to a diversity of situations. It is mostly used to cool buildings and reduce the enormous energy supply for air-conditioning. However, PRC can be beneficial to cool photovoltaic devices and improve the solar conversion efficiency and lifetime. For every 1 degree in temperature rise, the solar conversion efficiency of a silicon solar cell reduces by 0.45% relatively, and the lifetime will half every 10 degrees in temperature rise. Here, we see that PRC is based on the concept that heat can be dissipated via thermal radiation if the optical properties of your solar cell are chosen correctly. We will discuss the concept of PRC and conclude with a condition for the emissivity of the photonic structure for PRC for solar cells.

In order to understand the PRC concept, the thermal balance is examined of a solar cell. In Figure 2.1, a schematic representation of the energy balance is shown of a solar cell, with the four main powers that determine the equilibrium temperature of the cell: the irradiation from the sun (P_{sun}), the absorbed thermal radiation from the atmosphere (P_{atm}), the thermal radiation the solar cell is emitting (P_{rad}) and the power lost or gained by convection (P_{conv}). Here we assume that the conduction of heat via connection to the rooftop is negligible. The total cooling power is given by the sum of the four main powers,

$$P_{cool} = P_{rad} + P_{sun} + P_{atm} + P_{conv}. \qquad 2.1$$

When the total cooling power is zero, there is no net heat flux, and the solar cell has reached equilibrium temperature. The primary energy input is the irradiation from the sun, which is for normal incidence given by

$$P_{sun} = -\int I_{AM1.5}(\lambda)\alpha_{sc}(\lambda)d\lambda, \qquad 2.2$$

with $I_{AM1.5}$ the solar irradiation within AM1.5G[22] and α the absorptivity of the solar cell. In Figure 2.2a, the AM1.5G solar spectrum is shown and the bandgap energy of silicon is indicated. The AM1.5G solar spectrum has an integrated power of 1000 Wm[-2], but silicon does not absorb light with energies below its bandgap. Therefore, for further calculations, P_{sun} is set at 800 Wm^{-2}, which is the integrated power in the AM1.5G solar spectrum until the silicon bandgap (the yellow surface in Figure 2.2a).
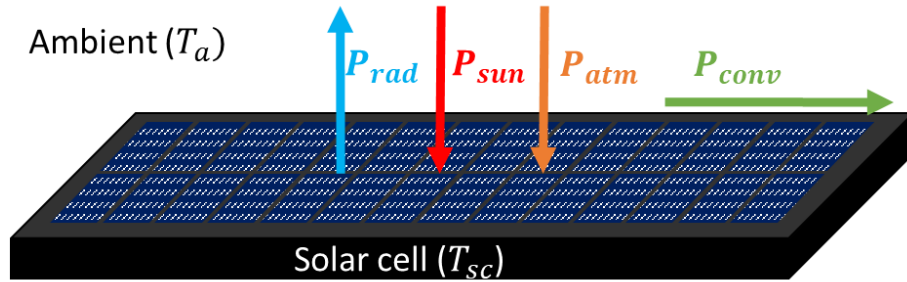

Figure 2.1: Schematic representation of the incoming and outgoing powers that determine the equilibrium temperature of a solar cell (T_{sc}). The solar cell reaches its equilibrium temperature when the power from the sun (P_{sun}) and the thermal radiation from the atmosphere (P_{atm}) are in balance with the thermal radiation emitted by the solar cell (P_{rad}) and the power flow by convection (P_{conv}).

Secondly, heat can be exchanged between the solar cell and its environment through convection, given by the product of the non-radiative heat transfer (h_c) coefficient with the temperature difference ($\Delta T = T_{sc} - T_a$),

$$P_{conv}(T_{sc}, T_a) = h_c(T_{sc} - T_a). \qquad 2.3$$

For a wind speed of 1 and 3 m/s, the non-radiative heat transfer coefficient is 6 and 12 $Wm^{-2}K^{-1}$, respectively[16]. Lastly, both the solar cell and the atmosphere radiate as a non-ideal blackbody. The emitted radiative power is given by

$$P_{rad}(T_{sc}) = \int I_{BB}(\lambda, T_{sc})\epsilon_{sc}(\lambda)d\lambda, \qquad 2.4$$

which is the product of the emissivity of the solar cell (ϵ_{sc}), a number between zero and one that determines the quality of the solar cell as a blackbody, and the black body radiation according to Planck's law[23]

$$I_{BB}(\lambda, T) = \frac{2hc^2}{\lambda^5}\frac{1}{e^{\frac{hc}{\lambda kT}}-1}. \qquad 2.5$$

The absorbed radiative power from the atmosphere is given by

$$P_{atm}(T_a) = -\int I_{BB}(\lambda, T_a)\epsilon_{atm}(\lambda)\alpha_{sc}(\lambda)d\lambda; \qquad 2.6$$

the product of the blackbody radiation from the atmosphere times the emissivity of the atmosphere (ϵ_{atm}), and the absorptivity of the solar cell (α_{sc}). Using Kirchhoff's law that states that for a body in thermal equilibrium, the emissivity equals the absorptivity at every wavelength

$$\epsilon(\lambda) = \alpha(\lambda), \qquad 2.7$$

it can be seen that the equations for emitted and absorbed thermal radiation both depend on the emissivity of the solar cell. The radiative cooling power is the sum of equations 2.4 and 2.6, resulting in

$$P_{cool_{rad}} = \int (I_{BB}(\lambda, T_{sc}) - I_{BB}(\lambda, T_a)\epsilon_{atm})\epsilon_{sc}(\lambda)d\lambda. \qquad 2.8$$
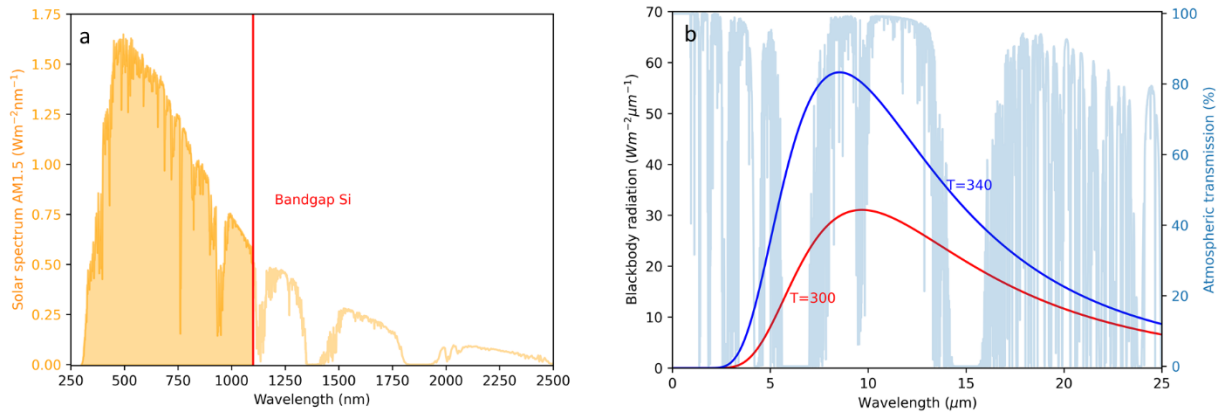

Figure 2.2: (a) AM1.5G solar irradiation spectrum (yellow line) as a function of wavelength, the bandgap of silicon (red line), and the part of the solar spectrum that can be absorbed by silicon (yellow surface). (b) Blackbody radiation spectra for an object at 300 K and 340 K in red and blue, respectively, with the atmospheric transmission in light blue.

The radiative cooling power depends on the difference between the blackbody radiation of a body at the temperature of the solar cell (T_{sc}) and the blackbody radiation of a body at the temperature of the atmosphere (T_a) times its emissivity. The emissivity of the atmosphere at normal incidence is given by[16]

$$\epsilon_{atm}(\lambda) = 1 - t_{atm}(\lambda), \qquad 2.9$$

where t_{atm} is the atmospheric transmittance (acquired through the Gemini Observatory Archive at NSF's NOIRLab[24]).

Figure 2.2b shows the atmospheric transmission with the blackbody spectra of a body at 300 K and 340 K, corresponding to ambient temperature and the approximated temperature of an operating solar cell, respectively. Since the integrand of equation 2.8 scales linearly with the emissivity, the radiative cooling power can be optimized by tuning this property of the solar cell.

The condition for the ideal emissivity for PRC for a solar cell is

$$I_{BB}(\lambda, T_{sc}) - I_{BB}(\lambda, T_a)\epsilon_{atm} \geq 1; \quad \epsilon_{sc}(\lambda) = 1$$
$$I_{BB}(\lambda, T_{sc}) - I_{BB}(\lambda, T_a)\epsilon_{atm} < 1; \quad \epsilon_{sc}(\lambda) = 0.$$

<div align="right">2.10</div>

Here, the offset of 1 is chosen to create a relatively smooth ideal $\epsilon_{sc}(\lambda)$ curve. Using Kirchhoff's Law (equation 2.7), the emissivity of an object can be computed using

$$\epsilon(\lambda) = \alpha(\lambda) = 1 - R(\lambda) - T(\lambda).$$

<div align="right">2.11</div>

Thus, the emissivity can be maximized by reducing the reflectance and transmittance.

First, we consider a case where an object is reflective. It does not absorb any solar irradiance and is in equilibrium with air at ambient temperature ($T_{eq} = T_a$). Using equations 2.8 and 2.9, the radiative cooling power is proportional to the transmittance of the atmosphere,

$$P_{cool_{rad}}(\lambda) \propto \left(I_{BB}(\lambda, T_{eq}) - I_{BB}(\lambda, T_{eq})\epsilon_a \right) \propto t_a(\lambda).$$

<div align="right">2.12</div>

This indicates a first-order condition for the emissivity: that the emissivity should be unity at wavelengths where the atmosphere is transparent - between 8 and 14 μm - and zero otherwise. This is also the target emissivity spectrum used by Raman et al. [16] in their photonic cooler design.

However, a silicon solar cell is not reflective, ideally, it is a perfect absorber for photons with higher energy than the silicon bandgap energy. Therefore, it is at a higher operating temperature than ambient. From Stefan-Boltzmann Law, we know that the total thermal emission of a blackbody is proportional to the fourth power of the temperature[25]. Consequently, the radiated power from the solar cell ($P_{rad}(T_{sc})$) will be higher than the incoming radiative power from the atmosphere ($P_{atm}(T_a)$). For a body that absorbs solar radiation, a first-order approximation for the ideal emissivity is given by the following three objectives: (i) absorption of solar light until the solar cell bandgap, $\epsilon_{sc}|_{280nm}^{\lambda_{bg}} = 1$; (ii) no absorption of solar light after the bandgap, $\epsilon_{sc}|_{\lambda_{bg}}^{4\mu m} = 0$, where the solar spectrum is assumed to end at 4μm wavelength; and (iii) a perfect black body after the solar spectrum, $\epsilon_{sc}|_{4\mu m}^{30\mu m} = 1$, until the end of blackbody spectrum at 340 K.

For a more detailed condition for the ideal emissivity for different silicon solar cell temperatures and wavelengths, equation 2.10 should be evaluated. This results in Figure 2.3, showing the ideal emissivity spectrum versus the solar cell temperature. A horizontal line in the figure shows a step-like spectrum ideal for PRC. The temperature of a perfect reflector will not exceed ambient temperature. Thus, the ideal emissivity of a perfect reflector is given by the solar cell at ambient temperature, 300 K. The result is unity emissivity in the two windows where the atmosphere is transparent, approximately 8 to 13 μm and 16 to 25 μm. For a solar absorber at 340 K, the ideal emissivity spectrum is unity from 3 to 30 μm wavelength.
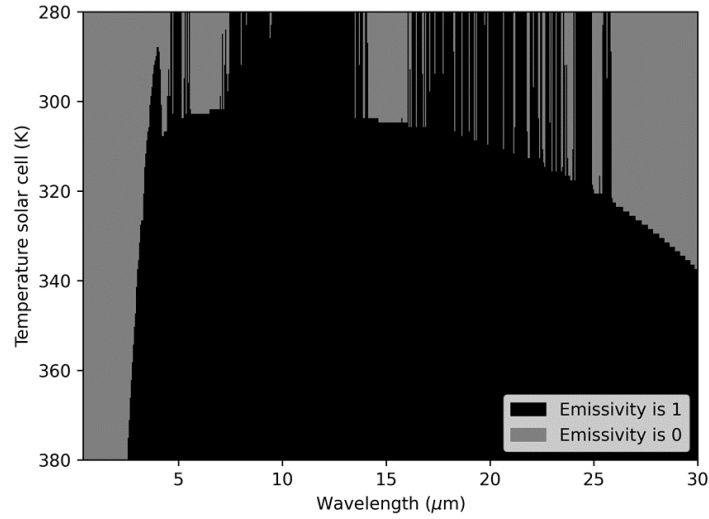
Figure 2.3: Colormap of the ideal emissivity spectrum versus the solar cell temperature, where the emissivity is 1 when the emitted thermal radiation is larger than the absorbed thermal radiation, computed with equation 2.10.

Figure 2.4a shows three theoretical emissivity spectra: zero emissivity (red), a non-zero emissivity only in the main atmospheric transmission window (green), and the ideal emissivity for a body at 340 K taken from Figure 2.3 (blue). The total cooling power can be calculated with these emissivity spectra according to equation 2.1, shown in Figure 2.4b. This figure shows the cooling power versus the temperature of the solar cell with a theoretical emissivity corresponding to Figure 2.4a at a solar irradiance of 800 Wm^{-1} and a non-radiative heat transfer coefficient of 6 $Wm^{-2}K^{-1}$. When the cooling power is positive, the outgoing power is higher than the incoming power – thus, the solar cell cools – and when the cooling power is negative, the incoming power exceeds the outgoing power – thus, the solar cell heats up. At the intersection where the cooling power is zero, the solar cell is at equilibrium temperature. For a solar cell with zero emissivity, both P_{rad} and P_{atm} are zero, and the equilibrium temperature is only determined by the balance between solar irradiance and convection. This results in an equilibrium temperature of 365 K, which is the upper boundary of the equilibrium temperature of a solar cell. Whereas, if the radiative cooling is optimally exploited, the equilibrium temperature is 330 K, shown in the blue line. This results in a potential cooling due to PRC of 35 degrees.
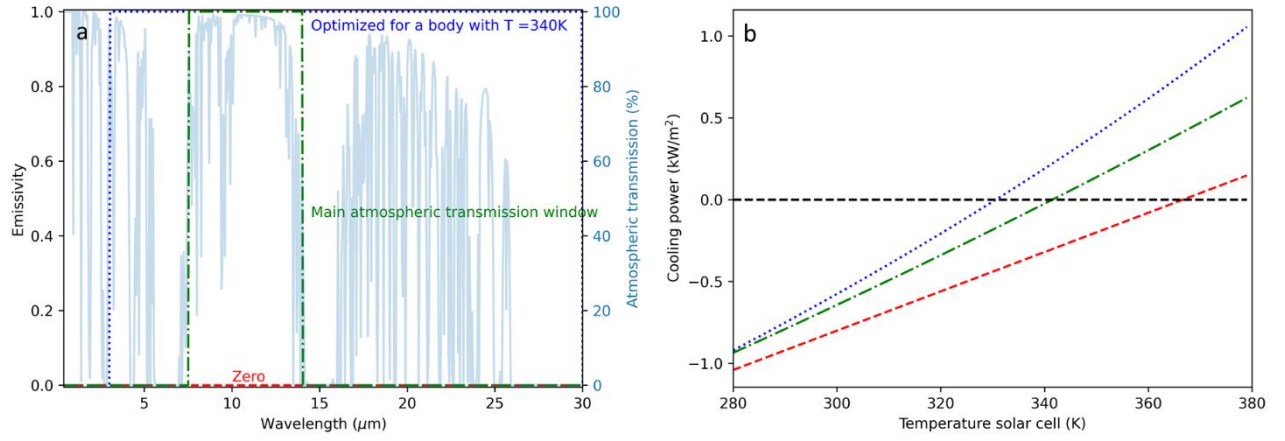
Figure 2.4: (a) Step function of three emissivity spectra: zero emissivity (red), a non-zero emissivity only in the main atmospheric transmission window (green), and the ideal emissivity for a body at 340 K taken from Figure 2.3 (blue). (b) the calculated cooling power versus temperature, assuming $h_c = 6\ Wm^{-2}K^{-1}$ and $P_{sun} = 800\ Wm^{-2}$, of a solar cell with an emissivity corresponding to (a). Equilibrium temperature is reached when the cooling power is zero.

3 Light theory and nanophotonic design

In Chapter 2, we have computed a condition for the ideal emissivity of our solar cell: a unity emissivity for wavelengths larger than 3 μm. First, general concepts in light-matter interactions are discussed to understand the behaviour of light propagating through a structured surface. Second, using general light theory, we will see that the radiative cooling property of silicon is poor and that this is already improved by adding the module glass used for protection. Therefore, the radiative properties are compared for several kinds of glass. Finally, we will use FDTD simulations to find and optimize two designs: one on top of a bare silicon solar cell and a second based on a silica-based solar module. For both designs, we improve the absorptivity in the infrared - and thus, by Kirchhoff's Law, the emissivity – by adding a photonic glass structure on the surface. For the bare silicon case, we optimize a close-packed array of microscopic glass spheres, where the multiple reflections due to the sphere's curvature are used to reduce the total reflectance. For the silica-based solar module, we design a texture of silica micro-cylinders, exploiting the forward scattering of specific Mie-like resonances.

3.1 Light-matter interactions

Light is an electromagnetic wave that satisfies Maxwell's equations. When this wave hits a plane of a different medium, there are two boundary conditions; the electric and magnetic field must be continues and so must the derivative of the electric and magnetic field. Solving Maxwell's equations at an interface with these boundary conditions returns the reflection and transmission amplitude of the light, better known as the Fresnel coefficients[23]. For a multilayer stack, the Fresnel coefficients can be transferred into the transfer matrix model (TMM). The light propagation at every interface is described in a matrix (M_n),

$$\begin{pmatrix} v_n \\ w_n \end{pmatrix} = M_n \begin{pmatrix} v_{n+1} \\ w_{n+1} \end{pmatrix}, \qquad\qquad 3.1$$

where v_i and w_i are the forward and backward propagating electromagnetic waves in the i'th layer[26]. The total system can be described with the product of the individual matrices

$$M_s = M_n M_{n-1} \dots M_2 M_1. \qquad\qquad 3.2$$

Throughout this thesis, a Python script is used for the TMM written by Steven Byrnes[26]. The script returns the total reflectance and transmittance for a stack of n layers with thickness d_n and complex refractive index $\tilde{n}_n$, with the incident plane wave under an angle with s or p polarization.

The complex refractive index describes the interaction between light and matter. The real part of the refractive index is the ratio of the speed of light in your medium with respect to vacuum speed of light ($n = v/c$)[23], while the imaginary part – the extinction coefficient – describes the absorptive behavior of the material. The extinction coefficient is the number of times that the light intensity is decreased by a factor e, per meter.

With TMM, Fabry-Pérot resonances in multilayers can be described. These occur because the reflected beams from the first or second interface have different phases upon exiting the stack, and they will interfere. The interference causes an oscillatory movement in the reflectance spectrum. Destructive interference, where the path difference is equal to half the wavelength of the light, results in minima, and constructive interference results in maxima in the reflectance spectrum. The first-order destructive interference occurs when the thickness satisfies

$$d_{FB} = \frac{\lambda_0}{2n} cos\,\theta_t, \qquad\qquad 3.3$$

where λ_0 is the free space wavelength of light, n is the refractive index and θ_t is the angle of the transmitted light inside the layer.

Light propagation through a parallel multilayer can be described using TMM. However, when the interface is not planar, other mechanisms manipulate the light that is not described by TMM. The behavior observed in light propagation mostly depends on the dimension of the structures (d) on the surface with respect to the

wavelength of the light, three regimes can be defined: (i) when the wavelength of light is much larger than the structures ($d \ll \lambda$), the behavior of light can be described by TMM, using an effective medium approximation to estimate the optical properties of the inhomogeneous layer, (ii) for wavelengths much smaller than the structures ($d \gg \lambda$) the interaction can be described by geometrical optics, and (iii) when the wavelength is in the same order of magnitude as the structures ($d \approx \lambda$) electromagnetic theory is needed to describe the light propagation properly[27]. To describe the propagation of light most accurately, a combination of all kinds of interactions is used.

3.1.1 Effective medium theory

In the first regime ($d \ll \lambda$), the light does not 'see' any individual structures. Therefore, the light propagation can be described with TMM using an effective index for the structured surface. The effective medium theory describes the refractive index of a layer that is composed of several materials. The Maxwell-Garnett model is the most used model to define the effective dielectric constant of a structure consisting of two materials with dielectric constants ϵ_1 and ϵ_2 with a mixing constant f. With the dielectric constant given by[28]

$$\tilde{\epsilon} = \epsilon + i\tilde{\epsilon} = n^2 = (n + i\tilde{n})^2,$$ 3.4

the Maxwell-Garnet effective medium (ϵ_{MG}) should satisfy[29]

$$\frac{\epsilon_1 - \epsilon_{MG}}{\epsilon_1 + 2\epsilon_{MG}} = f \frac{\epsilon_1 - \epsilon_{MG}}{\epsilon_1 + 2\epsilon_{MG}}.$$ 3.5

With the effective medium, general light theory can be used to describe the light propagation through a randomly structured inhomogeneous layer with smaller dimensions than the wavelength of light.

3.1.2 Geometrical optics

In the second regime, $d \gg \lambda$, the light is too small compared to the structures, and the propagation can be described using geometrical optics. In this method, light is treated as a particle rather than a wave, using the Law of Reflection – the angle of incidence is the angle of reflection – and Law of Refraction (Snell's law)

$$n_1 \sin \theta_1 = n_2 \sin \theta_2,$$ 3.6

that returns the angle of the transmitted light (θ_2) depending on the incidence angle (θ_1) and the refractive index of the first and second medium (n_1 and n_2, respectively). Using these two laws and the extinction coefficient of the media, all pathways of the light can be traced through the structures until all light is reflected, transmitted, or absorbed in the media. Geometrical optics can be used when the dimension of the structures is much larger than the wavelength of the light and interference effects are not taken into account.

3.1.3 Mie-like resonances

Finally, for the regime where $d \sim \lambda$, the light will polarize the structures, inducing resonant effects. These resonant eigenmodes are often called Mie-like resonances, described with the Lorentz-Mie-Debye solution of Maxwell's equations. Mie-theory describes the scattering of a high-index homogeneous spherical particle made of a dielectric or metallic material[30]. If the particle is not spherical, we still observe Mie-like resonances in photonic structures. It has been shown that silicon nanocubes and nanocylinders can support both electric and magnetic resonances and that the resonance wavelength can be tuned with the dimension of the particle[31]. The lowest order resonances - the electric and magnetic dipole - redshift with increasing particle dimension. As a rule of thumb, the dipolar resonances occur when $\frac{\lambda}{n} \sim d$; higher order modes can be found at smaller wavelengths[31].

Furthermore, it has been shown that the interference of the electric and magnetic dipole resonance can suppress backscattering and induces forward scattering of light[32]. This effect is maximal at the Kerker condition when the amplitude and phase of the electric and magnetic dipole are equal[33]. When a resonant particle is placed on a substrate, the light is scattered into the substrate. It has been shown that the proximity of a substrate broadens the resonant modes[31].

3.2 Photonic design

Using the theory for light-matter interactions, the radiative properties of a solar cell can be examined and a photonic cooler can be designed to meet the optimal condition to enhance PRC. Firstly, a suitable material must be chosen to reach an emissivity of 1 for wavelengths larger than 4 µm.

The optical properties are examined in the infrared (IR) for several common dielectrics in Figure 3.1: silicon (Si)[34], silica (SiO_2)[34], borosilicate[35], Soda Lime Glass (SLG)[36], silicon nitride (Si_3N_4)[37], aluminum oxide (Al_2O_3)[34], hafnium oxide (HfO_2)[28], and titanium oxide (TiO_2)[38]. For a suitable material for PRC, it must absorb in the IR. Examining Figure 3.1b, this rules out silicon as a radiative cooler, for its extinction coefficient is zero over the entire range. Furthermore, aluminum oxide, hafnium oxide, and titanium oxide show a strong extinction coefficient from a wavelength above 10 µm, while the blackbody radiation at 340 K peaks at 9 µm. Consequently, using these materials would not allow you to increase the emissivity at the peak wavelength. Silicon nitride shows a broad absorption peak covering the entire atmospheric transmittance window, which would make for a perfect radiative cooler. However, it turns out challenging to make a homogeneous layer of silicon nitride in the micron range thickness on top of silicon.

Lastly, the extinction coefficient spectra of several kinds of glass - silica, SLG, and borosilicate - show a strong absorption peak around 9 µm, caused by a Si-O asymmetric stretching mode in the crystal[39], precisely at the peak wavelength of the blackbody radiation at 340 K. This, together with their total transparency in the visible wavelength range, makes it a perfect material for PRC for solar cells. Additionally, most solar cells are encapsulated in glass for protection, making the application in the solar cell industry possible.

Because glass is a collective for multiple compositions, here we will narrow it down to two distinct kinds, silica, which is a pure SiO_2 crystal and Soda Lime Glass (SLG). From now on, we will refer to these as silica and SLG, respectively.
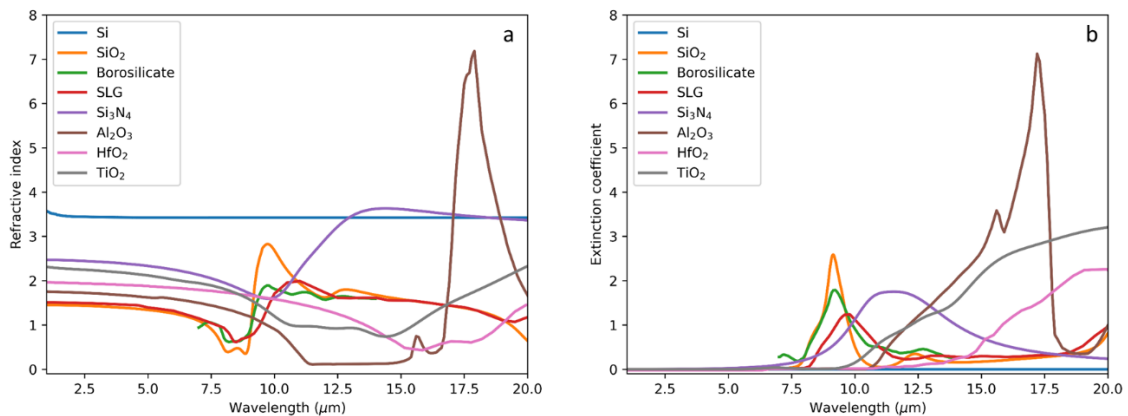

Figure 3.1: (a) The refractive index and (b) the extinction coefficient of the most prevalent materials in PV.

In order to confirm that silicon is a bad radiative cooler and to investigate the effect of the module glass, the reflectance and transmittance in the IR are calculated using TMM. Both for a bare silicon substrate and silicon covered with module glass. Figure 3.2 shows the reflectance and transmittance of a 500 µm-thick double-

sided polished (DSP) silicon slab with and without a 500 μm-thick layer of silica or SLG. For bare silicon, the transmittance shows that all light that is not reflected at the air-silicon interface is transmitted. The figure confirms that no light is absorbed in the silicon, indicating it as a bad radiative cooler. Adding a 500 μm-thick layer of silica or SLG on top shows total absorption in the IR, improving the radiative properties enormously. However, the large reflectance peak around 9 μm reduces the radiative cooling significantly: it coincides precisely with the peak wavelength of the blackbody radiation and lies within the atmospheric transparency window.
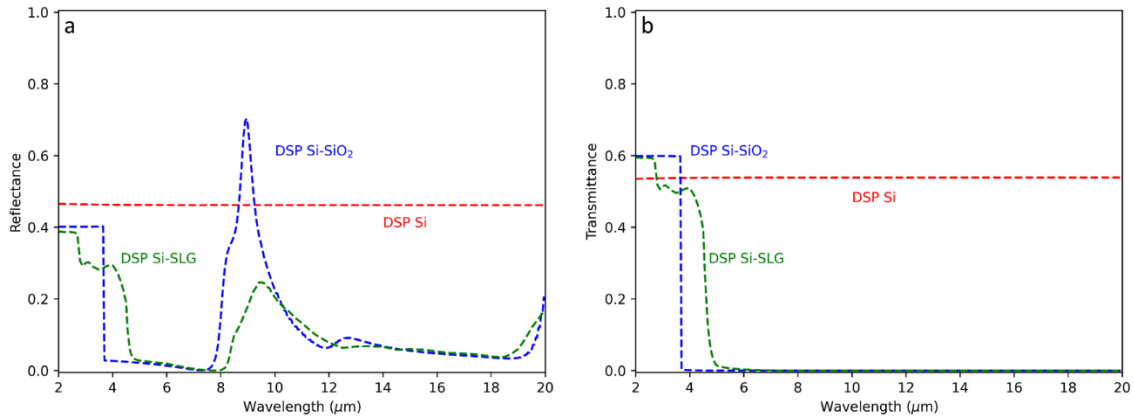

Figure 3.2: (a) the reflectance and (b) transmittance of 500 μm thick double-sided polished silicon (DSP Si) substrate (red), covered with 500 μm silica (blue) or soda lime glass (green).

Figure 3.3 shows the emissivity of bare silicon and after covered with the two kinds of glass, calculated with equation 2.11. This indicates that both types of glass already approach the ideal emissivity for a perfect absorber, the only possible improvement is the reduction of the reflectance peak around 9 μm. At the same time, silicon is close to the worst-case scenario for radiative cooling, i.e., zero emissivity. Consequently, two designs are proposed: one to improve the radiative cooling for a bare silicon solar cell, that should increase the absorption in the IR, and the other for a silica-based solar module, which is mainly made as an anti-reflection coating in the IR to reduce the dip in the emissivity spectrum caused by the first-order reflection. Because all solar cells have a metal back contact that covers the entire back of the solar cell, we exclude transmission by coating our samples with gold. This simplifies the optimization by making an effective anti-reflection coating in the IR for both designs.
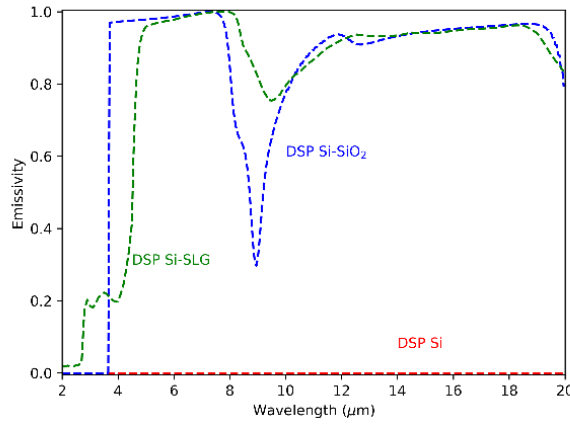
18

Figure 3.3: The calculated emissivity spectra (1-R-T) of a bare double-sided polished silicon (DSP Si) substrate coated with gold (red) and covered with 500 μm silica (blue) or soda lime glass (green). The emissivity of DSP Si is zero in the entire infrared wavelength range, indicating it as a bad radiative cooler.

3.2.1 Anti-reflection coating

In the visible wavelength range, anti-reflection (AR) is a very well understood concept used to improve solar absorption. The simplest way to reduce the reflection of a silicon slab is to use a single layer anti-reflection coating. For a typical silicon solar cell, this is typically a layer of Si_3N_4 on top of the silicon. This layer induces Fabry-Pérot resonances, where the light reflects from both Si- Si_3N_4 interfaces. Calculating this for a silicon nitride layer on top of silicon results in an optimal thickness of 80 nm. This method would be applicable in the IR, but Fabry-Pérot resonances only occur at a distinct wavelength and cannot be used for a broadband AR effect.

A second well-known AR coating for silicon solar cells is random inverted pyramids in the geometrical optics regime; this ensures multiple reflections at the air silicon interface before the light can escape. Random inverted pyramids increase broadband light absorption by suppressing average reflectance from 35 to 10 percent[40]. This would be effective in the IR if silicon were to absorb in that wavelength range.

Lastly, resonant nanostructures are used to trap light. Silicon nanopillars have shown a tunable reflectance spectrum over the entire visible wavelength range by combining Fabry-Pérot with Mie resonances[41]. Nevertheless, a nanopillar exhibits only discrete resonant modes, making it hard to apply as a broadband AR coating for solar cells. On the other hand, using silicon nanocones, the resonance wavelength varies with height, enabling broadband absorption in the entire visible wavelength range[42]. To achieve AR in the IR, we base our design on the last concept: resonant structures are used to combine several concepts in light-matter interactions in order to achieve broadband AR.

Because of the fabrication challenge to make dielectric microstructures on top of silicon, we chose to base our design for bare silicon on a coating of glass spheres, which can be deposited using one of several techniques[43–45]. For the AR coating for a solar cell module, it is possible to etch a geometry into the silica glass, so we chose a design of an array of cylinders. To further optimize our design for an AR effect in the IR, Finite Difference Time Domain (FDTD) simulations are used. They are performed in Lumerical FDTD Solutions.[46]

3.2.2 Bare silicon design and optimization

The simulation setup for an AR coating designed for bare silicon solar cells is an array of silica spheres on a silicon substrate. An incidence plane wave source is placed 6 μm above the structures. The reflectance and

transmittance are measured 1 μm above the plane wave and 1 mesh under the substrate surface, respectively (see Figure B.1 for the configuration). The simulation is run under symmetrical boundary conditions at a mesh of 100 nm and a minimum auto-shutoff of 1e-5 (for the mesh, auto shut-off convergence, see Figure C.1). The difference between s- and p-polarized incidence light is negligible, so the simulation is only run at one polarization.

To reach optimal light trapping, the radius of the particles is varied around the dimension where the dipolar resonances would be expected, from a radius of 1 to 15 μm. The pitch is varied as a multiple of the radius, as the minimal pitch is twice the radius. The figure of merit (FOM) is the total cooling power, given by equation 2.1, where the emissivity of the solar cell is approximated by $1 - R$ and the temperature at 340 K. Shown in Figure 3.4, the optimal geometry for light trapping for a silicon substrate is found to be a close-packed hexagonal array of silica spheres with a radius of 10 μm. This geometry reaches a cooling power of 415 W/m^2, a significant portion of the maximum of 460 W/m^2 corresponding to the ideal emissivity.
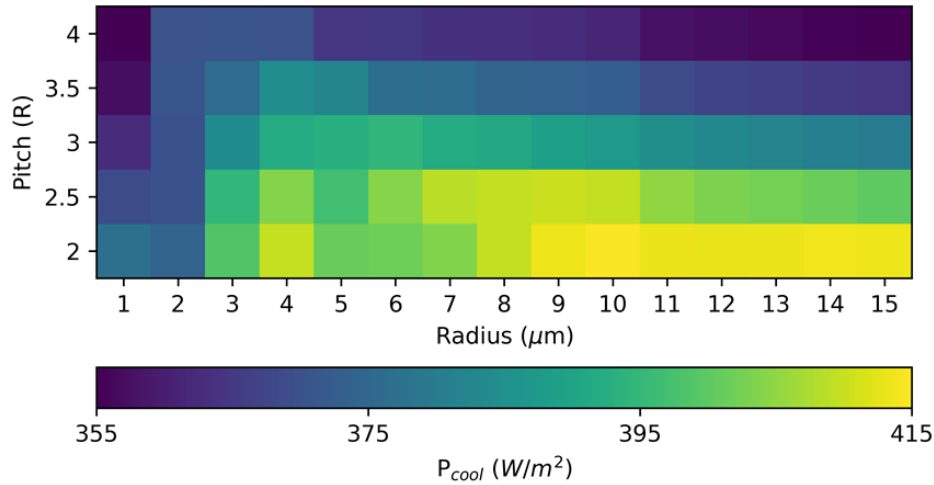

Figure 3.4: Color map of a sweep of the radius and the pitch of a hexagonal array of silica spheres on top of silicon, where the figure of merit is the calculated cooling power of structure based on the emissivity spectra acquired with Lumerical ($\epsilon = 1 - R$). The ideal geometry is found to be a close-packed monolayer of silica spheres with radius 10 μm, resulting in a theoretical cooling power of 415 W/m^2 out of the theoretical maximum of 460 W/m^2.

To calculate the total reflectance of the stack – a gold-coated silicon substrate covered with a monolayer of spheres – we use the Helmholtz reciprocity principle that states that the transmittance through a path will be equal for light traveling the same path in the opposite direction[47]. In our case, this would mean that a normal incidence plane wave traveling from the substrate through the monolayer would result in the same total transmittance as with incidence light from the top. Assuming that all light is transmitted in a specular direction, the total reflectivity can then be calculated by using the transmitted light through the top layer as input for the transfer matrix model, and the total reflectance is given by

$$R_{tot} = R_{FDTD} + R_{sub}T_{FDTD}^2 + R_{sub}^2 R_{FDTD}T_{FDTD}^2 + \cdots, \qquad 3.7$$

where R_{sub} is the reflectance calculated with TMM for a three-layer stack: 500 μm silicon, 80 nm of gold and air. Because our structures are highly absorbing, we only take the first two reflection terms from equation 3.7 into account. Furthermore, we make the assumption that all light is transmitted or reflected specular, which is not the case over the entire IR range (see Appendix A).
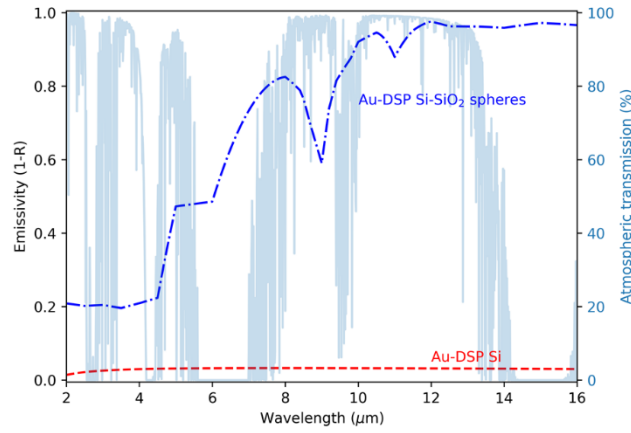
Figure 3.5: Calculated emissivity spectrum of a stack of double-sided polished silicon coated with gold (Au-DSP Si), bare (red), and with the optimized geometry of close-packed silica spheres on top with a radius of 10 μm (red), with the atmospheric transmittance in light blue. The total emissivity of silicon is improved by adding the spherical glass coating, especially in the atmospheric transmittance window.

Figure 3.5 shows the resulting calculated emissivity spectrum of the geometry, with bare silicon coated on the back with gold, as a reference, against the atmospheric transmittance. It shows that the emissivity is significantly increased by the monolayer of glass spheres, especially from 8 μm wavelength, precisely where the atmosphere is transparent and where the blackbody radiation of 340 K peaks.

3.2.2.1   Geometrical ray tracing

The resulting geometry of our stack is a layer of close-packed spheres with a radius of 10 μm. This is in the regime where the dimension of the particle exceeds the wavelength of light and the reflectance and transmittance can be computed using geometrical ray tracing. In Figure 3.6, the three possible pathways of incidence light are shown, and for every regime an approximation can be made of the total reflectance of the light. First, light that hits the surface at a smaller angle than 45 degrees (red) will have a single reflectance at the silica interface before escaping. The total reflectance of this part (45.4%) of the incoming light can be approximated by the reflectance of a layer of silica on silicon at normal incidence because angle-dependent reflection for angles smaller than 45 degrees is insignificant. Light that hits the surface at a larger angle (blue) will have a minimum of two reflections before escaping. The multiple reflections will decrease the total reflectance significantly, so this part of the incoming beam (45.3%) is effectively trapped between the spheres and will eventually be absorbed, resulting in no reflectance. Finally, light entering precisely between the spheres (orange) will have a single reflection on the air-silicon interface (9.3%).
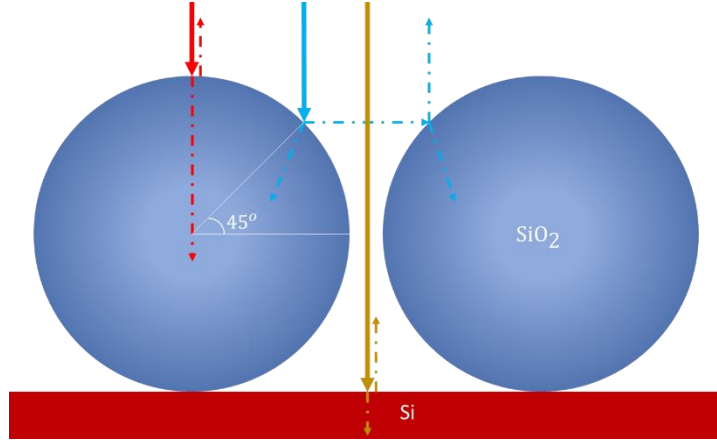
Figure 3.6: Schematic representation of ray tracing for the coating of spheres on silicon. Three possible pathways of incident light are shown; light at incoming light hitting a surface at less than 45 º will have a single reflectance before escape (red), incident light hitting the surface at higher incidence angle will have minimal two reflections before escaping (blue) and light incidence between the sphere reflects at normal incidence at the silicon substrate (yellow).

3.2.3   Silica-based solar module design and optimization

For the silica-based solar module design, the simulation configuration is a hexagonal array of silica cylinders on silica, using a mesh of 25 nm and a minimal auto-shutoff of 1e-7. The same simulation setup and optimization steps are done for the design based on a cylindrical coating for silica-based solar module glass (see Figure B.2: Configuration of cylindrical design in Lumerical, (a) top view and (b) side view. and Figure C.2: Convergence test of cylindrical geometry of SiO_2, (a) the mesh convergence and (b) the minimal auto-shutoff convergence. for configuration and convergence test, respectively). However, this geometry has an extra parameter that has to be optimized: the height. First, the height is set equal to the radius, which together with the pitch are varied, resulting in Figure 3.7a. Next, the height is varied versus the radius at the optimal pitch (3.5 times the radius), and the ideal geometry is found: a hexagonal array of cylinders, a radius of 1.75 µm, a height of 2.25 µm, and a 6.125 µm pitch. With this design, a potential cooling power can be reached of 450 W/m^2, which closely approaches the maximum of 460 W/m^2 based on the ideal emissivity. Furthermore, from Figure 3.7b, the robustness of the design is shown: a defect in the fabrication would still work.
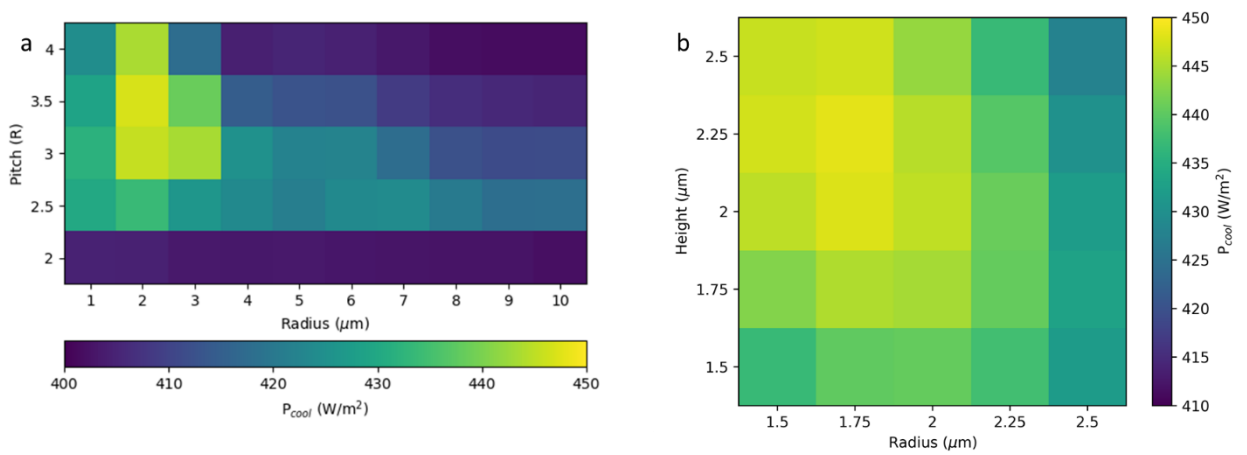

Figure 3.7: Colormap of the optimization of the geometry of a hexagonal array of silica cylinders on silica, where the figure of merit is the calculated cooling power of structure based on the emissivity spectra acquired with Lumerical (e = 1-R). (a) Radius/height versus pitch sweep and (b) a radius versus height sweep at the optimal pitch of 3.5 times the radius. The optimal geometry is found to be a hexagonal array of cylinders (radius 1.75 µm and height 2.25 µm) at a pitch of 6.125 µm. Resulting in a cooling power of 450 W/m^2 out of the theoretical maximum of 460 W/m^2

Using equation 3.7, the resulting calculated emissivity is shown in Figure 3.8 against the atmospheric transmittance and with the unpatterned stack as a reference. By adding the pattern to the top of the glass, the emissivity dip is reduced, improving the radiative properties of the stack.
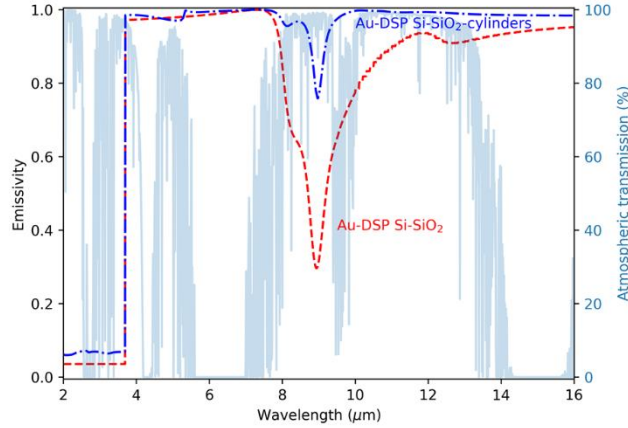

Figure 3.8: Calculated emissivity of a stack of double-sided polished silicon (DSP Si) coated with gold, with a silica layer on top (red) and with a patterned silica layer (blue) with the optimized geometry of silica cylinders (radius of 1.75 μm, height of 2.25 μm and a pitch of 6.125 μm), with the atmospheric transmittance window in light blue. The patterned module glass reduces and narrows the emissivity dip of glass at 9 μm, improving the radiative cooling of the stack.

3.2.3.1   Multipole decomposition

The optimized geometry for the array of cylinders is precisely in the range where we would expect dipolar resonances to occur ($d \sim \lambda$). To further investigate if these resonances occur and how they improve the absorptive property of the stack, multipole decomposition can be used. The multipole decomposition method enables us to determine which modes are excited by the incident light. Originally described by Mie theory, this was derived for spherical particles. Here, a theorem of Evlyukhin et al.[48] is used to calculate the multipole decomposition of non-spherical particles.

First, the polarization induced by a plane wave scales linearly with the total electric field inside the particle ($\boldsymbol{E}$),

$$\mathbf{P} = \epsilon_0(\epsilon_\mathrm{p} - \epsilon_\mathrm{d})\mathbf{E}. \tag{3.8}$$

This relation depends on the vacuum dielectric constant (ϵ_0), times the relative dielectric permittivity of the nanoparticle (ϵ_p) minus that of the surrounding medium (ϵ_d), which is 1 for air. To calculate the induced polarization inside the particle, the total electric field ($\mathbf{E}$) can be extracted from Lumerical simulation using a normal-incidence plane wave. The total time-averaged extinction power is given by the volume integral of the in-product between the incident electric field ($\boldsymbol{E}_0^*(\boldsymbol{r})$) with the induced polarization [49]

$$\mathrm{P_{ext}} = \frac{\omega}{2}\mathrm{Im}\int_{V_s}\boldsymbol{E}_0^*(\boldsymbol{r}) \cdot \boldsymbol{P}(\boldsymbol{r})d\boldsymbol{r}. \tag{3.9}$$

After substituting the different contributions of the modes, the total extinction power can be subdivided into the contributions of the different modes: electric dipole (P_{ext}^p), magnetic dipole (P_{ext}^m), electric quadrupole (P_{ext}^Q), and the toroidal dipole (P_{ext}^T):

$$\mathrm{P_{ext}} \cong P_{ext}^p + P_{ext}^m + P_{ext}^Q + P_{ext}^T. \tag{3.10}$$

To take higher order modes into account, it can easily be extended. The extinction cross-section can be computed by dividing equation 3.9 by the total incident power, resulting in a multipole decomposition of the

extinction cross-section, shown in Figure 3.9. The total extinction cross-section is shown of a micro cylinder in air, together with the contributions of the different modes: magnetic dipole (MD), electric dipole (ED) together with the toroidal dipole (TD), and the electric quadrupole (EQ). The total extinction coefficient is given by the sum of the scattering and absorption coefficient[48] and compares well to the sum of the contributions. This confirms our approximation to not involve any higher-order modes than the EQ. Two peaks are shown in the extinction cross-section, both of which are determined mainly by the ED, in combination with the EQ and MD in the first and second peaks, respectively.
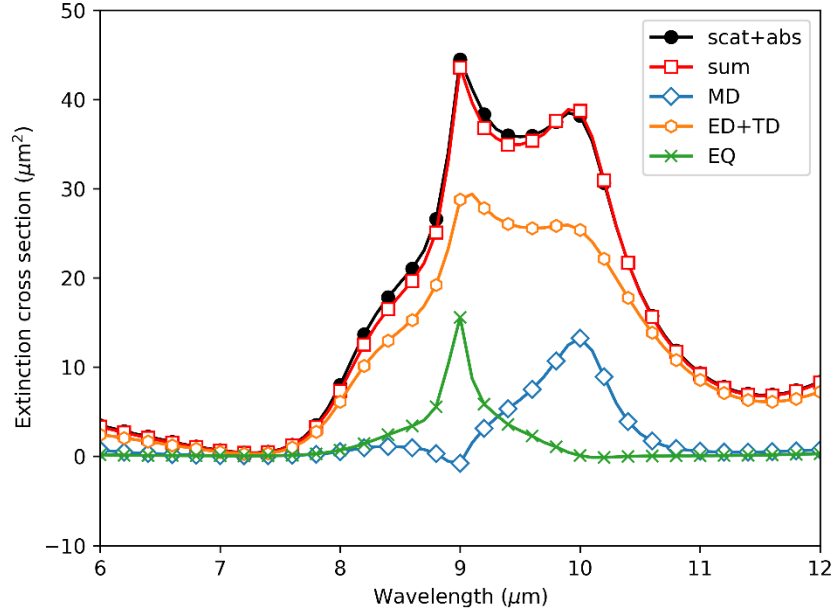

Figure 3.9: Multipole decomposition of a silica cylinder (radius 1.75 µm, height 2.25 µm), where the contribution is shown of several resonances of the total scattering cross-section. The resonance induced in the silica cylinder is determined mainly by the electric dipole.

The Kerker condition states that directional emission is achieved when the ED and MD mode have the same amplitude and phase. This will cause destructive interference in the backscattering plane. From Figure 3.9, we see that this is not the case for our cylinders, for the ED mode is stronger in the entire range than the MD mode. However, the Kerker condition can be generalized by taking the higher-order EQ mode into account, which is also strong in our geometry. Using the expressions from Aleaa et al.[33], the extinction cross-section can be divided into forward and backward scattering cross-section, shown in Figure 3.10. It shows that the forward scattering is much larger than the backward scattering.
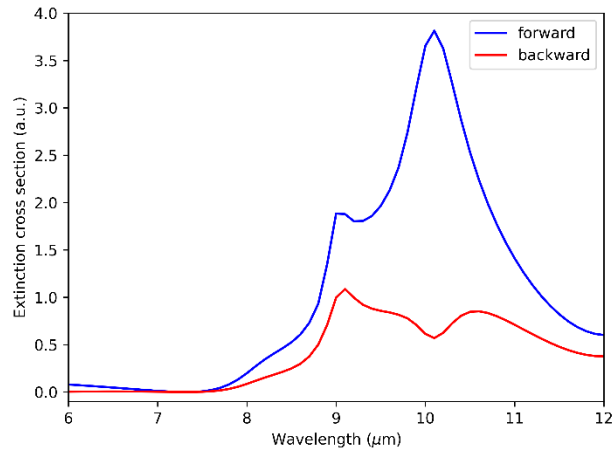
Figure 3.10: Forward (blue) and backward (red) part of the extinction cross-section of a silica cylinder (radius 1.75 μm, height 2.25 μm).

4 Fabrication and measurement

Based on the theory and simulations of Chapter 3, we fabricated the two approaches for PRC; one for bare silicon solar cell and the other for a solar module. Even though different methods are used to fabricate the spheres and the cylinders, the basis of the stack is identical: a double-sided polished silicon wafer coated with gold on the back. First, continuous convective deposition is used to coat a DSP Si substrate with a close-packed monolayer of glass spheres. However, we will see that using this method to make a homogeneous monolayer is challenging. Consequently, we switched to drop-casting to make a homogeneous monolayer. Next, UV-lithography and reactive ion etching are used to fabricate the cylindrical pattern on the silica module glass. Finally, the samples are imaged using an optical microscope as well as an SEM.

4.1 Fabrication

A DSP Si wafer (WRS Materials) is used with a thickness of 500 μm that is lightly n-doped with phosphorus with a resistivity of 1-20 Ωcm^{-1}. The wafer is cut into 24x24 mm^2 pieces and cleaned for 15 minutes in a base piranha solution. Afterward, it is submerged into isopropanol and blow-dried with a N_2 gun. Next, E-beam physical vapor deposition (EB-PVD) is used to deposit 80 nm of gold on the silicon substrates. EB-PVD occurs in a vacuum chamber where a crucible with gold is heated using an electron beam. The vapor spreads through the room and condenses on the silicon substrate, creating a homogeneous gold layer. A vibrating crystal is used to measure the mass deposited and thus the thickness of the layer. These gold-coated DSP Si substrates serve as a basis for all samples. Next, we used two different methods for the two approaches for radiative cooling: the monolayer of spheres on silicon is made bottom-up, while a top-down process is used to etch the cylinders into a silica substrate.

4.1.1 Self-assembled monolayer

There are several possible ways to make a monolayer of spheres on top of a substrate, like dip-coating, continuous convective deposition, drop-casting, or spin-coating. Because of the dimensions of our particles (diameter of 20 μm), continuous convective deposition and drop-casting are the most feasible methods.

4.1.1.1 *Continuous convective deposition*

Figure 4.1 shows the schematic representation for continuous convective deposition. The substrate is placed horizontally on a motorized stage which can move in the x-direction with a speed from 1 to 1000 μm per minute. The deposition blade is positioned at an angle of 5 degrees and approximately 50 μm above the substrate. The deposition blade is silanized, making it more hydrophobic. The substrate is moved to the left with deposition speed (v_d) while keeping the deposition blade in place. A vacuum pump keeps the substrate horizontal, preventing any movement caused by the forces exerted by surface tension of the suspension. The stage is connected to a Peltier to control the temperature of the stage, either sub- or super ambient.
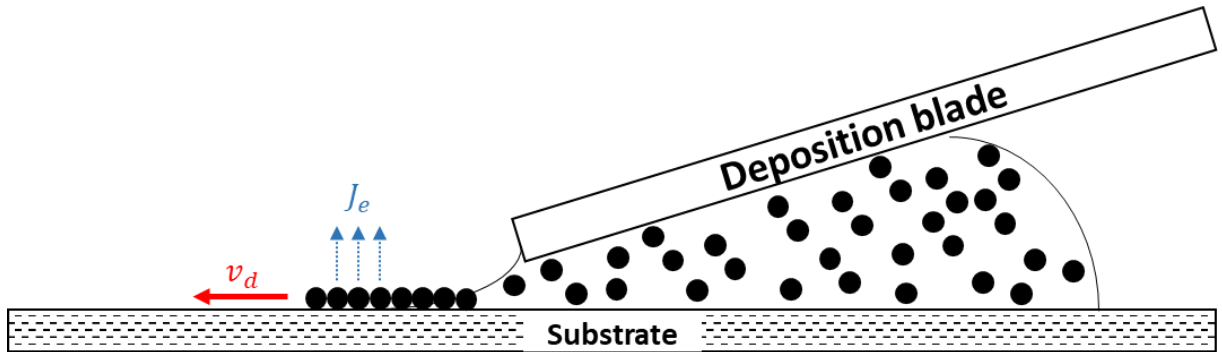

Figure 4.1: Schematic representation of the continuous convective deposition setup used to make a self-assembled monolayer of spherical particles.

In continuous convective deposition, a meniscus forms between the tip of a hydrophobic blade and the hydrophilic substrate (see Figure 4.1). The curvature of this meniscus depends on the distance between the blade and the substrate, the properties of the solvent, and the hydrophilicity of the substrate.

During the deposition, a balance exists between the pressure in bulk solution and in the wetting film in the meniscus. In an atmosphere saturated with water, evaporation is made impossible, and a mechanical equilibrium is established. The pressure in the meniscus is the sum of the van der Waals and electrostatic disjoining pressures and the capillary pressure due to the curvature of the liquid between two particles. In equilibrium, this is equal to the reference capillary pressure[50].

When evaporation starts, the mechanical equilibrium is broken. The evaporation flux (j_e) will induce an influx of suspension from the bulk into the wetting film that consists of a water component (j_w) and a particle component (j_p). The total amount of evaporated water $(J_e = l j_e)$ is precisely compensated by the total amount of water that enters the meniscus $(J_w = h_f j_w)$. Resulting in a water component given

$$j_w = \frac{l j_e}{h_f}. \qquad\qquad 4.1$$

The particle component (j_p) scales linearly with the water flux[50],

$$j_p = \frac{\beta \phi}{1 - \phi} j_w. \qquad\qquad 4.2$$

The scaling factor depends on the volume fraction (ϕ) and a proportionality coefficient (β) depending on the particle-particle interactions and particle-substrate interactions. Due to the particle flux, the particles will accumulate in the film. When the deposition speed of the film is zero, the particles will keep accumulating in the film, and a multilayer of particles is observed. The array growth rate $(v_c [m/s])$ is the product of the particle flux $(j_p [m^3/s])$ with the height at the deposition front, divided by the total volume of particles per unit area in the deposited layer (V_p),

$$v_c = \frac{h_f j_p}{V_p}. \qquad\qquad 4.3$$

For the deposition of a monolayer of particles, the deposition speed should equate to the growth rate of the monolayer, and the substitution of equations 4.1 and 4.2 in equation 4.3 results in

$$v_d = v_c = \frac{\beta l \phi}{V_p (1 - \varphi)} j_e. \qquad\qquad 4.4$$

For a hexagonally packed monolayer, the volume of particles per unit area is $0.605 d$[50] with d the diameter of the particles, and βl is a constant to be experimentally determined. Then, the withdrawal rate of the substrate is estimated by rewriting equation 4.4 as[45]

$$v_d = \beta l \frac{j_e \phi}{0.605 d (1 - \phi)}. \qquad\qquad 4.5$$

From this equation, some conclusions can be drawn. Firstly, when the size of the particles increases (d), the withdrawal rate should decrease. Furthermore, when the volume fraction (ϕ) increases, the withdrawal rate should increase. Finally, when the evaporation rate (j_e) increases, the withdrawal rate should increase. The evaporation rate can be increased in several ways. For example, the substrate can be heated, the deposition can be done in a less humid environment, or a different solvent can be used. The evaporation rate of, for example, ethanol is higher than that of pure water[51].

Using equation 4.5, the deposition parameters can be optimized to deposit a monolayer on the substrate. However, during the deposition, fast accumulation and sedimentation were observed of the spherical glass particles, making this technique less suited for our deposition because a homogenous suspension is vital. This is probably caused by the large mass and the low hydrophobicity that increases the particle-particle interactions.

4.1.1.2 Drop casting

The second technique is drop-casting. When a droplet of suspended particles evaporates from a surface, three types of depositions can be observed: a ring of deposited particles, a small bump in the middle, or a uniform layer (see Figure 4.2). The deposition depends on the strength of different types of convective flows in the droplet. The coffee ring effect is caused by a radial convective flow induced by the higher evaporation at the edge of the droplet[52]. The accumulation of the particles in the center of the droplet is caused by recirculatory Marangoni flow caused by a temperature gradient induced by the latent heat of evaporation[53]. Lastly, a uniform layer will be observed when there is a strong interaction of the particles with the substrate, causing convection towards the substrate[54]. This effect is even increased when the substrate is made more hydrophilic due to the reduced contact angle. Because of the large dimension of our spherical particles, the attractive force between the particles and the substrate is assisted by gravity and can be further enhanced by activating the surface of the substrate with UV/ozone treatment.
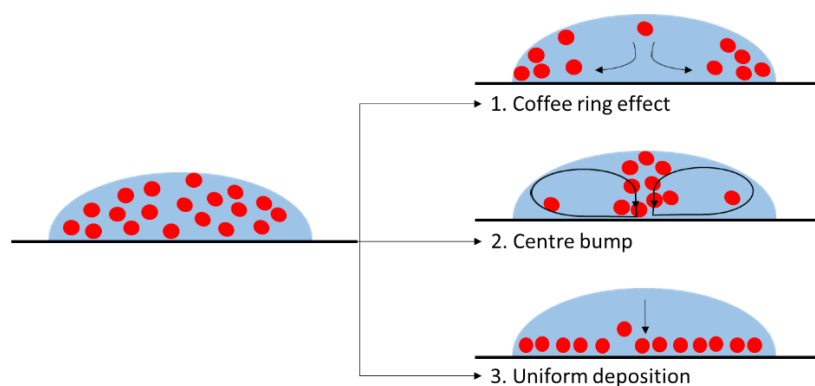

Figure 4.2: Three deposition forms of drop-casting: coffee ring effect, deposition in the center, and a uniform deposition over the surface.

The spherical design for a coating for silicon solar cells is made on top of the basis gold-coated silicon wafer that is cleaned for 10 minutes with a UV ozone cleaner (BioForce UV/Ozone ProCleaner). In the UV ozone cleaning, the oxidizing agent atomic oxygen is used to clean and activate the surface, making it more hydrophilic. In the chamber, two wavelengths of light are used, 184 and 253 nm. The first wavelength is absorbed by oxygen, creating ozone. The 253 nm wavelength light is responsible for the destruction of ozone. In the UV box, ozone is continuously being formed and destroyed. In the destruction of ozone, the activated oxygen will react with all contaminants on the surface. This will also result in a prolonged increase of the polar surface energy, increasing the wettability[55]. For UV ozone cleaning to work, it is essential to use clean samples without any organics since this will react in the UV box.

The suspension of microspheres was made by suspending the number of spheres needed to cover a 24x24 mm surface of borosilicate spheres (Thermo Fisher Scientific, 9000 series) in 200 μL demineralized water. Note that our design was originally based on silica spheres; borosilicate glass has a slightly different refractive index (see Figure 4.1). According to the manufacturer, the spheres have a density of 2.55 g/cm^3 and an average diameter of 22.2 ± 0.9 μm, instead of the 20 μm diameter we aimed for. The suspension was sonicated using a Branson 2800 Cleaner for 15 minutes right before it was deposited on the activated silicon substrate.

Subsequently, the substrate was dried in a closed box under lab conditions: a humidity of 40% at an ambient temperature of 20 degrees Celsius. The silicon substrate was kept at a constant temperature of 17 degrees Celsius to minimize the radial convection due to evaporation and to ensure uniform deposition.

The schematic representation of the total coated stack for bare silicon is shown in Figure 4.3a. The fabricated sample, using drop-casting, is imaged from the top with a camera (Figure 4.3b), and an optical image is taken with a Zeiss Axioskop (Figure 4.3c). A self-assembled monolayer can be recognized by a distinct hexagonal packing from the top. Nevertheless, this is not apparent, caused by the high inhomogeneity of the diameter of the spheres. Furthermore, the inconsistency in color might indicate an inhomogeneity in the glass composition. By imaging at different focal depths, we determined that the grey area in Figure 4.3b is a single layer of spheres on the Si substrate, while the white part is a multilayer.
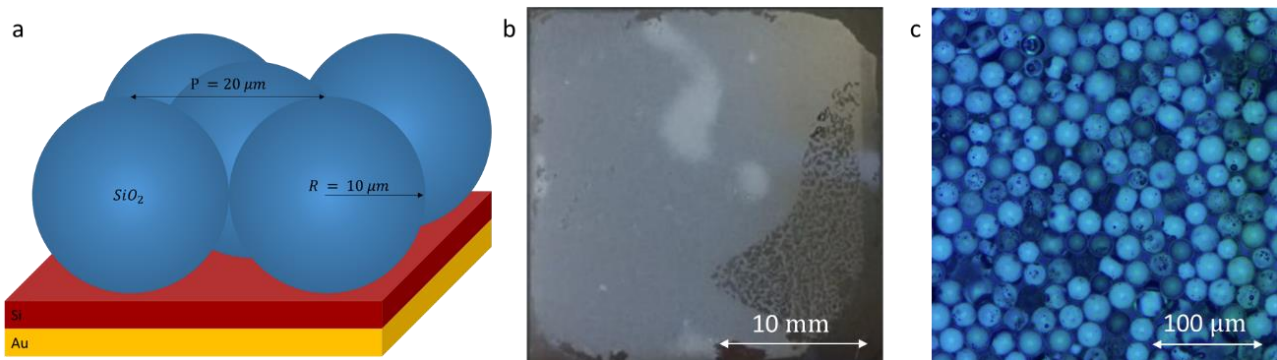

Figure 4.3: (a) Schematic representation of the optimized geometry for radiative cooling for silicon and (b) an image from the top of the sample, and (c) a microscopic image from the sample.

4.1.2 UV lithography and reactive ion etching

The design for the solar module is a hexagonal array of silica cylinders on top of silica (see Figure 4.4a). The cylinders are etched into a silica wafer with UV lithography and reactive ion etching. This is placed on top of the gold-coated DSP Si substrate using immersion oil as a refractive index matching fluid. For the reference, silicon with three types of glass is examined, 500 μm silica, 1000 μm SLG, and 500 μm borosilicate glass.

First, a 4", 500 μm thick silica wafer (Siegert wafers) is cleaned for 15 minutes in base piranha, immersed into isopropanol, and blow-dried with a N_2 gun. An HMDS layer is used for adhesion between the substrate and the resist. We spin-coated a monolayer with a Süss MicroTec Delta 80, using a spin speed of 4000 rpm for 45 seconds. Subsequently, the substrate is baked at 150 $^{\circ}$C for 1 minute. Next, 2 micron of a negative photoresist (Ma-N 1420) is spin-coated, with a spin speed of 2000 rpm for 30 seconds, and baked at 100 $^{\circ}$C for 2 minutes. The disadvantage of spin-coating is that at low spin speed, like 2000 rpm, it is likely that some resist accumulates at the edge of your wafer. In the next step, this will prevent a proper illumination of the resist because vacuum contact is needed. To remove the edge beat, the outer 5 mm of the 4" wafer is dipped into edge beat removal fluid.

The grating in the photoresist layer was fabricated using a UV mask aligner (Süss MicroTec MABA6). A 4" mask (Delta Mask BV), made of glass with a thin patterned layer of chrome on top, is placed in contact with the substrate under vacuum and is used to selectively illuminate the resist with 365 nm wavelength light. The light improves the ability of the photoresist to resist the developing agent. The back of the substrate is covered with blue tape before illumination to avoid backscattering interference. After illumination, the substrate is immersed into the developing agent, MAD 533s, for 75 seconds to etch off the unilluminated photoresist.

The grated photoresist works as an etch mask for the reactive ion etching. Using an Oxford PlasmaPro Cobra ICP/RIE, the silica was etched in high vacuum and room temperature with an inflow of equal amounts of C_4F_8 and Argon, for 16 minutes and 30 seconds to achieve the cylinder height of 2.25 μm. Next, the remaining photoresist is removed by acetone and base piranha. Finally, the wafer is cut into 24x24 mm^2 substrates.

A schematic representation of the optimized stack is shown in Figure 4.4a. An image from the fabricated structure with a camera (Figure 4.4b) shows the sample is still transparent in the visible range. From the optical image (Figure 4.4c), we can see that the hexagonal array of cylinders is homogeneous over a large area, and the geometry of the sample is measured using an SEM, showing the crosscut taken with an FEI Helios 600 DualBeam (Figure 4.4d). The diameter was measured at 3.65 μm and the height 2.20 μm, which corresponds to the optimized design. However, several SEM images were taken (Appendix D), showing that the geometrics depended on the place on the 4" wafer; the agreement between fabricated and optimized geometry decreased to the edge of the sample.
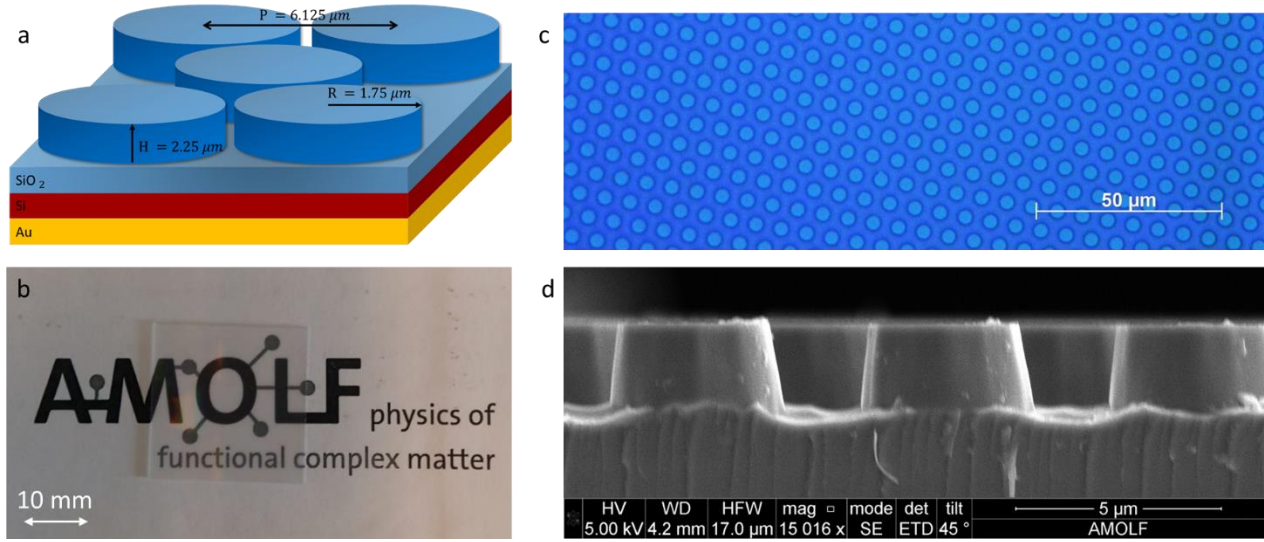

Figure 4.4: (a) Schematic representation of the optimized geometry for radiative cooling for glass, (b) a picture from the sample from the top, (c) a microscopic image from the top of the sample, and (d) an SEM image of the crosscut.

4.2   Optical measurement

To examine the emissive properties in the IR, infrared hemispherical reflection measurements were used. The infrared hemispherical reflection measurements were conducted in the modified Bruker Vertex70 research-grade laboratory FTIR spectrometer at the University of Twente (see Appendix E), as described in the work by Hecker et al.[56] The Vertex70 is modified with an external, custom-made integrating sphere with a diffuse gold coating, with a Mercury Cadmium Telluride (MCT) mid-infrared detector on top. The sample is positioned at the south pole of the sphere, with a variable aperture of maximum 20 mm. An external, high-power Globar light source was used for high signal-to-noise measurements.

Measurements are taken at a wavenumber resolution of 8 cm-1 and repeated 8 times to average out the noise. Depending on the sample's surface, scattering or flat, the measurement is normalized to the reflection of a diffuse or flat gold substrate, respectively, and a measurement with an open sample port is used to subtract the background signal.

Furthermore, to measure the absorptivity in the visible wavelength range, hemispherical reflectance measurements were conducted in the VIS to NIR as well. An integrating sphere with a diffuse Teflon coating in reflection configuration was used to capture all light reflecting from the samples. A supercontinuum laser was coupled into the integrating sphere, and the reflected light was measured with a spectrometer.

The hemispherical reflectance was measured over a wavelength range from 600 to 1600 nm. Because of the large wavelength range, two spectrometers are used with different configurations. In the VIS, the reflectance was measured with 200 ms exposure time, 150 grating lines per mm were used with a blaze of 500 nm. In the NIR, the exposure time was 1 second, with 150 grating lines per mm and a blaze of 1200. Furthermore, to exclude higher-order grating effects, all short-wavelength light was blocked, using a long-pass filter of 650 nm and 1050 nm for the wavelength range 600-1100 nm and 1100-1600 nm, respectively.

5 Result and discussion

To validate the concept obtained by the FDTD simulations in Chapter 3, we did hemispherical reflectance measurements on the fabricated samples in both the IR and the VIS wavelength range. Additionally, we measured the influence of several types of module glass on the emissivity of the stack. The measured emissivity is computed as one minus the hemispherical reflectance. The measured emissivity is compared to the calculated emissivity, using a combination of FDTD and TMM with the optical constants shown in Figure 3.1. Finally, the total cooling power versus temperature is calculated using the measured emissivity spectra. At the temperature where the total cooling power is zero, the solar cell is at equilibrium temperature.

5.1 Bare silicon solar cells design

Figure 5.1a shows the measured (solid) and computed (dashed) emissivity of the coated and uncoated silicon in blue and in red, respectively (see Figure 4.3a for the stack). The atmospheric transmission is plotted in light blue. The dashed lines are computed using a combination of FDTD and TMM (equation 3.7). In blue, the emissivity calculated using the optical constants of silica (SiO_2), is shown, and in purple, the optical constants of SLG are used because the optical constants of borosilicate were only available between 7 and 14 μm.

The emissivity of lightly doped silicon varies between zero and 30 percent over the entire wavelength range and shows some distinct peaks corresponding to Si-Si vibrations[57]. These features are not apparent in the dashed line, corresponding to the computed emissivity spectrum based on the optical properties from the Handbook of Optical Constants of Solids by Palik[34]. They do compare, however, to reported FTIR transmittance measurements[57,58]. The coated silicon (solid blue line) has an increased emissivity, especially in the window where the atmosphere is transparent.

The computed emissivity spectrum using the optical constants of silica shows some resonance features not present in the measured spectrum. The cause for this discrepancy is that the refractive index of silica shows higher and narrower vibrational modes than that of SLG (see Figure 3.1). When we compare the measured to the computed emissivity where the optical constants of SLG are used, the spectra compare better.

Finally, there is a discrepancy between the simulated and the fabricated geometry. In Figure 4.3b, the optical image from the top shows a significant deviation in the diameter of the spheres. For a resembling simulation, the standard deviation of the diameter can be determined from the picture, and a simulation would be built with a random distribution of spheres with the same deviation. This would blow up the simulation space enormously, and therefore is out of the scope of this study.

Figure 5.1b shows the measured absorptivity of the coated stack in blue and the uncoated reference in red. The solar spectrum is plotted in light orange. This indicates that any cooling effect is not due to worse incoupling of solar light into the solar cell. The figure even shows a slight increase in absorptivity, indicating that the coating also results in a slight AR effect in the visible wavelength range.
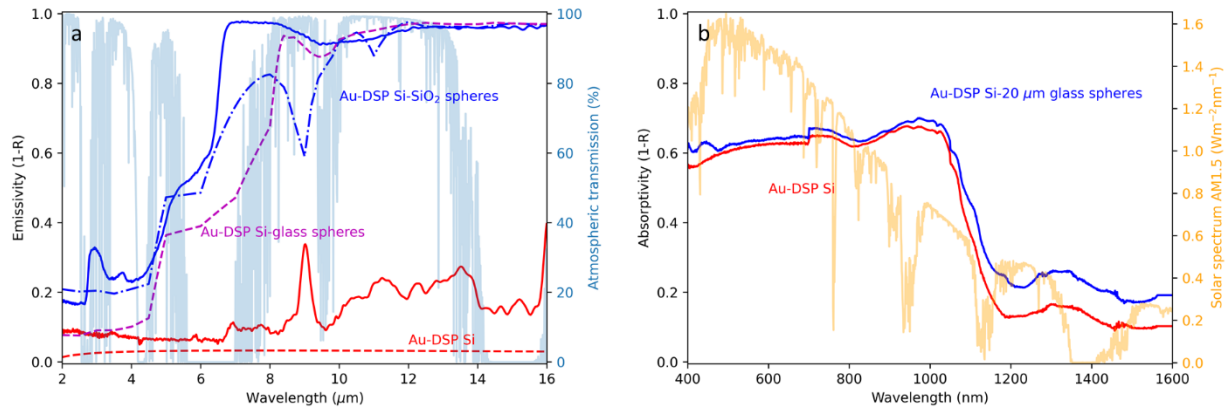
Figure 5.1: Measured (solid) and calculated (dashed) emissivity/absorptivity of double-sided polished (DSP) silicon coated with gold (red) and covered with SiO_2 spheres (blue) or SLG sphere (purple), (a) in the IR, and (b) in the VIS wavelength range.

5.2 Silica-based solar module design

Figure 5.2a shows the measured (solid) and calculated (dashed) emissivity patterned stack in blue, with the unpatterned stack as a reference in red. The emissivity dip of silica is significantly reduced by adding the pattern, increasing the average emissivity. The measured emissivity compares well with the calculated one, from 4 µm wavelength. For smaller wavelengths, there is most likely due to some missing information in the used refractive index values of silica from the Handbook of Palik[34]. The absorptivity in the visible wavelength range, shown in Figure 5.2b, is not reduced by adding the patterning to the module glass; it even shows a slight increase. This indicates that the light incoupling in the visible wavelength range is not reduced by our pattern.
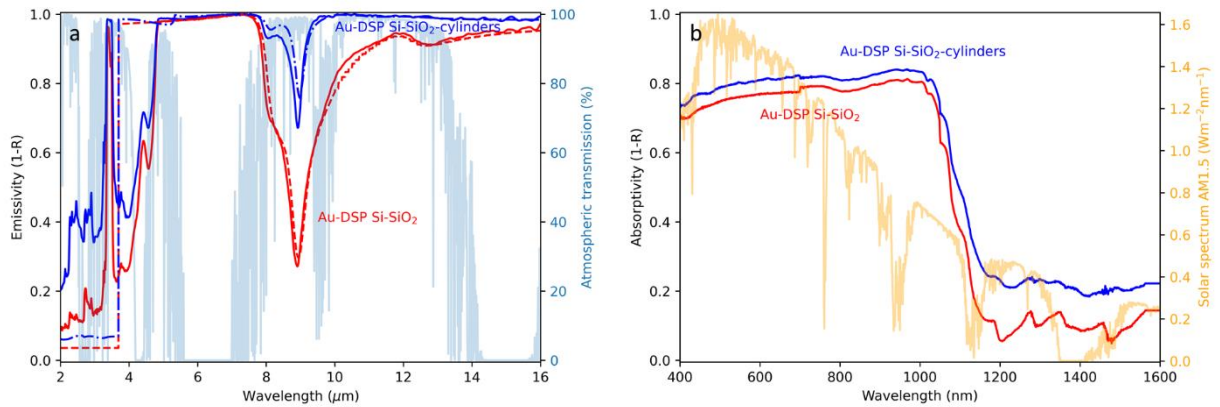

Figure 5.2: (a) Measured (solid) and calculated (dashed) emissivity/absorptivity in the IR and (b) VIS of gold coated double sided polished (DSP) silicon with a slab silica on top (red) and with patterned silica on top with cylinders (blue).

To further investigate the reason for the slight increase in absorptivity, the diffuse transmittance is measured of bare silica and the patterned silica with the same setup as the reflection measurements in transmittance configuration, without the gold-coated silicon underneath, shown in Figure 5.3. The transmittance of both bare silica as the patterned silica is approximately 90 percent over the entire range, the other 10 percent is due to the 4 percent reflectance at the two silica-air interfaces. It shows that the transmittance of bare silica does decrease due to the patterning. One reason for the contradiction between Figure 5.2 and Figure 5.3 could be caused by the trapping of some light inside the glass substrate because of high angle transmittance. If the

silica was on top of the silicon, this light would more easily be absorbed in the silicon, while without the silicon, it is more likely to escape from the top surface of the patterned silica.
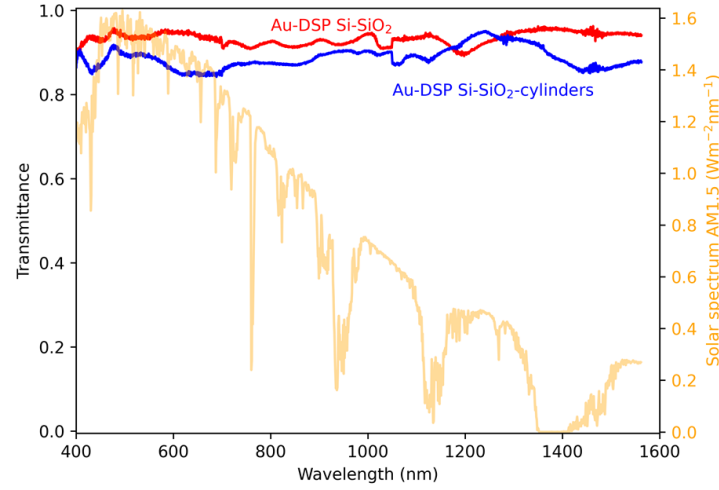

Figure 5.3: Measured transmittance in the visible wavelength range of bare silica and the patterned silica in red and blue, respectively. In yellow, the solar spectrum is plotted as a reference.

5.3 Comparison of module glass

From the previous paragraph, we have seen that the patterning of the silica module glass improves the PRC without having an impact on the incoupling of visible light. However, the module glass of silicon solar cells is typically not made of pure silica, but of a glass composition, like borosilicate or SLG. To investigate the contribution of our structure to the radiative cooling rate of a typical solar module, several types of module glass are compared. Figure 5.4 shows the measured (solid) and calculated (dashed) emissivity of a stack with three kinds of glass: silica, borosilicate, and SLG in blue, purple, and green, respectively. Note that the refractive index data for borosilicate is only available between 7 and 14 µm, which is interpolated to the wavelength boundaries. The atmospheric transmittance is plotted in light blue, and the emissivity of bare silicon in red. The silicon covered with silica shows a significant emissivity dip around 9 µm, caused by the first-order reflection from the top surface. This dip is less apparent in both SLG (green) and borosilicate glass (purple); they show a lower and more broadened emissivity dip. This difference mirrors the variance in the refractive index; the refractive index of silica shows a high and narrow peak, while both borosilicate and SLG have a lower and broadened peak due to different vibrations in the crystal.
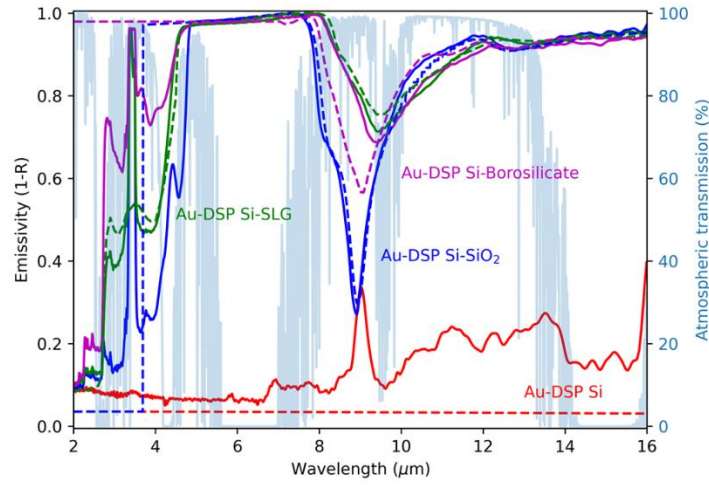
Figure 5.4: Measured (solid) and calculated (dashed) emissivity in the IR of double-sided polished (DSP) silicon coated with gold (red), with on top a slab silica (blue), soda-lime glass (green), and borosilicate (pink).

When comparing the stack with patterned silica with the stack with borosilicate or SLG glass, we see that the dip in emissivity for both cases is approximately 0.75. The cylinders improve the emissivity slightly by narrowing the dip, compared to the borosilicate and SLG glass. However, if we want to use the same patterning for an SLG-based solar module, a new optimization of the cylinders would be needed, and the PRC could even be maximized further.

5.4   Radiative cooling power

Using the measured emissivity spectra from the previous paragraph, the total cooling power can be calculated using equation 2.1 at solar irradiance of 800 Wm^{-1} and the non-radiative heat transfer coefficient of 6 $Wm^{-2}K^{-1}$. Figure 5.5 shows the total cooling power for the four sample stacks: bare silicon (red), silicon-coated with 20 μm glass sphere (blue), stack with unpatterned silica (green), and the stack with patterned silica (purple). The blue background shows the minimal and maximal contribution of the radiative cooling on the total cooling power (calculated in Figure 2.4). First of all, Figure 5.5 confirms the poor radiative cooling power of bare silicon, which is close to no PRC. Secondly, looking at the zoom-in, we can see that the coating of spheres and the cylinders improve the cooling power with respect to their reference, bare silicon, and silicon covered with unpatterned glass, respectively. The intersections, where the cooling power is zero, return the equilibrium temperature of our stack: 360 K, 338 K, 339 K, and 336 K, for silicon, coated silicon, stack with unpatterned silica, and stack with patterned silica, respectively. This shows a potential cooling of 22 degrees for the bare silicon solar cell and 3 degrees for the silica-based solar module.
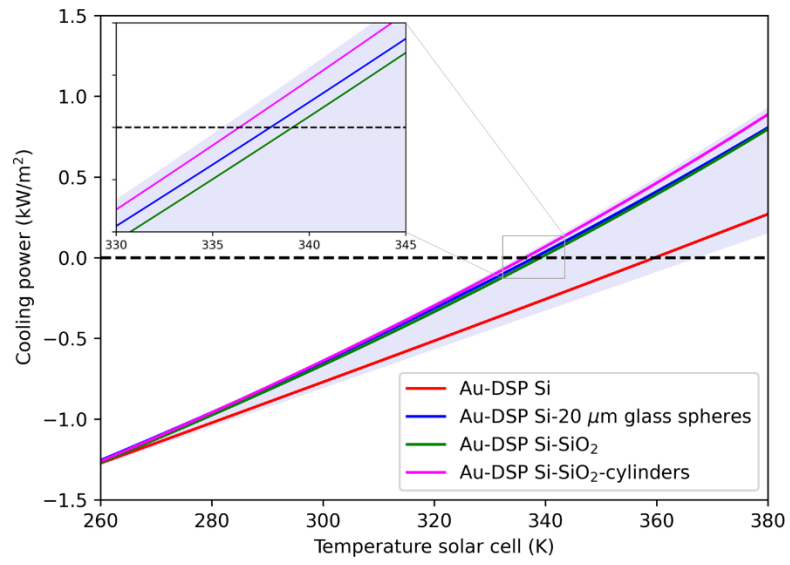
Figure 5.5: Calculated cooling power versus temperature of an object with the measured emissivity, red and blue the emissivity of bare silicon and of silicon coated with a monolayer of spheres (from Figure 5.1a), and in green and pink the emissivity of a silicon-silica stack with and without the patterning (from Figure 5.2a).

6   Temperature measurements

In the previous chapters, we have fabricated the radiative cooler designs, both for the bare silicon and for the silica-based solar module. From the hemispherical reflectance measurements, we have seen that the emissivity is improved by adding the structures on top and that the measurements compare well to the expected emissivity spectra. Next, we want to test the total cooling power of our samples. This is done by a rooftop experiment: using a thermocouple, the temperature of the four samples is measured under direct sunlight in Amsterdam. We will see that the coating of spheres reduces the temperature of the silicon significantly but that there is a large deviation on the measured temperature of identical samples. Consequently, we first measure the temperature of bare silicon, add the patterned and unpatterned silica, and compare the equilibrium temperature in time.

6.1   Measurement setup

The rooftop measurement apparatus is built from a Styrofoam box with four 24x24 mm^2 notches to hold the sample (see Figure 6.1). A thermocouple is connected to the back of each sample with copper tape to ensure proper heat transport. Next, the box is covered by cling film to minimize the non-radiative heat transfer coefficient (h_c). This design ensures that any material in contact with the samples or the air pocket surrounding the samples, heats up minimally. Subsequently, the box is put on the roof of AMOLF in Amsterdam, and the temperature of the four samples is measured using a calibrated thermocouple for one hour.

Figure 6.1: Temperature measurement apparatus on the AMOLF rooftop in Amsterdam on a partly cloudy day.

Figure 6.2: Temperature measurement on AMOLF rooftop of the coating of glass spheres on silicon (red), with three silicon reference measurements (green, blue, orange). shows the preliminarily measured temperature done on the AMOLF rooftop. First, the temperature of four samples was measured for one hour: three bare silicon samples (blue, green, and orange) and the coated silicon with glass spheres (red). After one hour, one of the silicon samples was covered with silica (orange) and one with patterned silica (green). We used immersion oil as a refractive index matching fluid. This allows us to compare the temperature of the covered silicon with the temperature before we added the silica on top.

When we first compare the bare silicon with the silicon coated with glass spheres, we see that during the entire measurement, the coated silicon was significantly lower than all three reference samples; 9 degrees cooling is achieved on average. However, a large deviation is observed between the identical silicon samples.

The difference between the blue and the green line is 0.2 degrees on average, and the orange line is on average 2.5 degrees lower than blue.

This indicates that the measurement conditions are not identical for all the samples, making the comparison a bit tricky. The reason for this difference can be that the thermocouple is not attached properly to the sample with lower temperature or that the conditions in the box are different for the four sample spots, i.e., convection. For further measurements, this should be improved.

Next, we compare the temperature difference after covering the silicon with the patterned and unpatterned silica. It is remarkable that the bare silica reduces the temperature of the silicon significantly, with approximately 6 degrees compared to before the silica was put on top. However, we would expect the patterned silica to work at least as well and even slightly better. This is not apparent from the measurements, we see that the patterned silica does decrease the temperature by approximately 3 degrees, but the improvement is less than the unpatterned silica.

One reason for this could be that the thermal contact was different for the two samples. We used immersion oil to make thermal contact between the silicon and the silica. However, this is a fluid, and after the measurement, a shift of the oil was observed. Because the improved cooling is mostly due to the dissipation of heat from the silica, bad thermal contact between the silicon and silica will prevent this.

Furthermore, the measurement was done on a partly cloudy day in Amsterdam, accounting for the large dip in temperature around 15:00 and between 16:15 and 16:30. For an improved measurement, we have to wait for better weather conditions and repeat the measurements a few times to check for reproducibility.
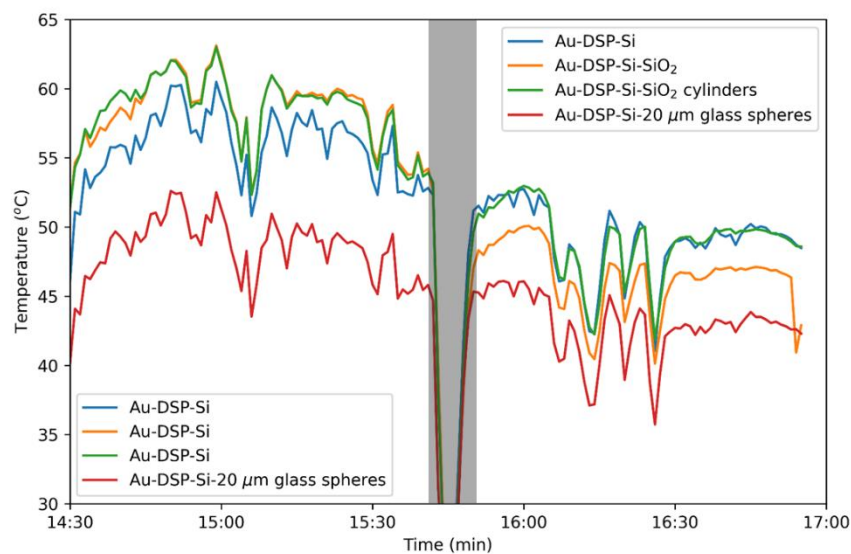

Figure 6.2: Temperature measurement on AMOLF rooftop of the coating of glass spheres on silicon (red), with three silicon reference measurements (green, blue, orange).

6.2 Outlook on IV measurements

For further understanding of PRC for solar cells, the electric power generation of the solar cell could be measured with and without the photonic cooling layer. The total generated electricity depends on more factors than only the temperature and from our optical measurements in the visible wavelength range, we see that the incoupling of light is altered by our structures, however not reduced. Because the mechanisms in the visible and infrared wavelength cannot be uncoupled, the total effect of our structures on the electric power generation of the solar cell should be measured by measuring the generated power, IV-curve, or open-circuit voltage of a solar cell while it heats up.

7 Conclusion and outlook

In conclusion, we have shown that a silicon solar cell can be cooled using PRC by photonic microstructures on the surface. Reducing the operating temperature of a solar cell is important because both the efficiency and its lifetime increase with temperature. By examining the thermal balance of a solar cell at T=340K, we compute the ideal infrared (IR) emissivity to be unity for wavelengths between 4 and 30 um. Next, two silica microstructures are designed and fabricated to improve the PRC of solar cells; one for a bare silicon solar cell and a second for a silica-based solar module.

For the first design, bare silicon is covered with a close-packed monolayer of microscopic silica spheres with a radius of 10 um to increase the IR emissivity. The glass spheres were made of borosilicate glass with a diameter of 22.2 um and by drop-casting, a uniform monolayer is deposited on a silicon substrate. The emissivity in the infrared of the fabricated stack is measured using a hemispherical reflectance measurement with an FTIR and compares well to the simulated FDTD results. The discrepancy is mostly caused due to the inhomogeneous glass spheres observed in microscopic images and due to the unknown refractive index of the glass spheres.

The second design is a patterning of the top layer of a silicon-silica stack with cylinders. Using UV lithography in combination with reactive ion etching, silica microstructures are fabricated. The measured hemispherical reflectance also compares well to the simulated design. A flat silica top layer shows a strong reflection peak around 9 um that is significantly reduced from 70 to 30 percent by the microstructures. For a silicon solar cell covered with a less pure glass than silica, such as SLG or borosilicate glass, the photonic cooling design can be re-optimized.

Finally, the temperature reduction is shown by a preliminary temperature measurement of our samples on the AMOLF rooftop under direct sunlight. For the silicon substrate coated with the glass spheres, an average temperature decrease of approximately 9 degrees is shown with respect to the bare silicon reference. However, a large temperature variation was observed between identical silicon samples of around 2.5 degrees. Next, the temperature is measured of the bare silicon and compared to the temperature of silicon covered with flat or patterned silica. Covered with the flat silica, the temperature decreased by approximately 6 degrees, while covered with the patterned silica, the temperature drop was approximately 3 degrees. Additional temperature measurements under very well controlled conditions are needed to establish a definitive temperature comparison between the samples.

7.1 Outlook

The microstructure design for a silica-based solar module can be applied to every kind of solar cell that is encapsulated in quartz silica glass to reduce its temperature. For other kinds of module glasses, the design should be re-optimized. Furthermore, the concept of passive radiative cooling can be applied to all outdoor devices that would benefit from a lower operating temperature.

A. APPENDIX: Diffuse and specular part of transmittance

In the calculations of the total emissivity of our two designs, the assumption is used that the transmitted light through the structure is mostly specular. In Figure A.1 and Figure A.2, the contributions of specular and diffuse transmittance is shown of the spherical and cylindrical geometry, respectively. Here, for the specular contribution, the integral is taken of the hemispherical far-field transmittance for light with angles smaller than 5 degrees from normal. Both figures show that the transmitted light from the structures is mostly diffuse. However, due to the high absorptivity of silica, most light is already absorbed before it hits the silica-silicon interface. Therefore, we consider the used assumption valid for both configurations.
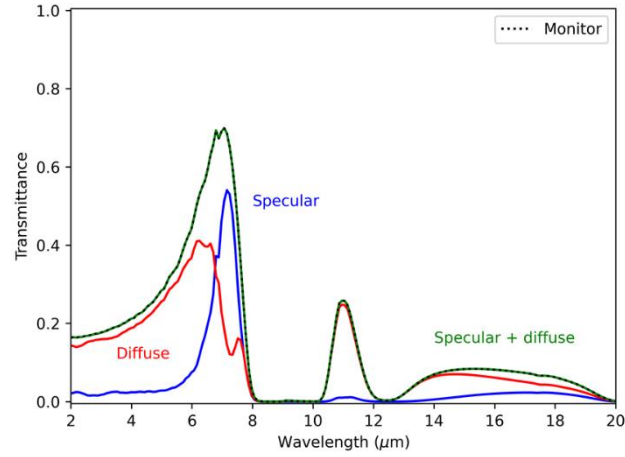

Figure A.1: Farfield transmittance of the monolayer of SiO_2 spheres. The specular part of the transmittance (blue), the diffuse part (red), the sum of these (green), and the measured transmittance with the power monitor (dashed).
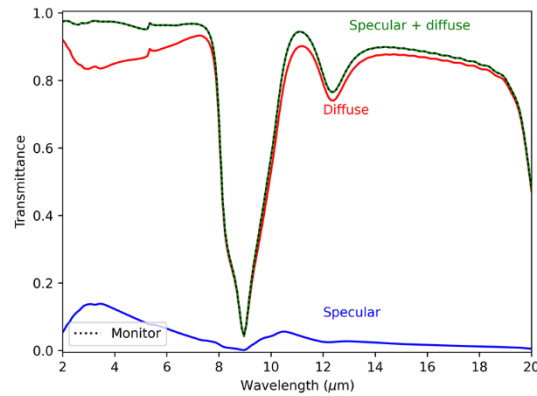

Figure A.2: Farfield transmittance of the hexagonal array of SiO_2 cylinders on SiO_2. The specular part of the transmittance (blue), the diffuse part (red), the sum of these (green), and the measured transmittance with the power monitor (dashed).

B. APPENDIX: Lumerical simulation setup

Figure B.1 and Figure B.2 show the setup of the spherical and cylindrical configuration in Lumerical, from top view (a) and side view (b).
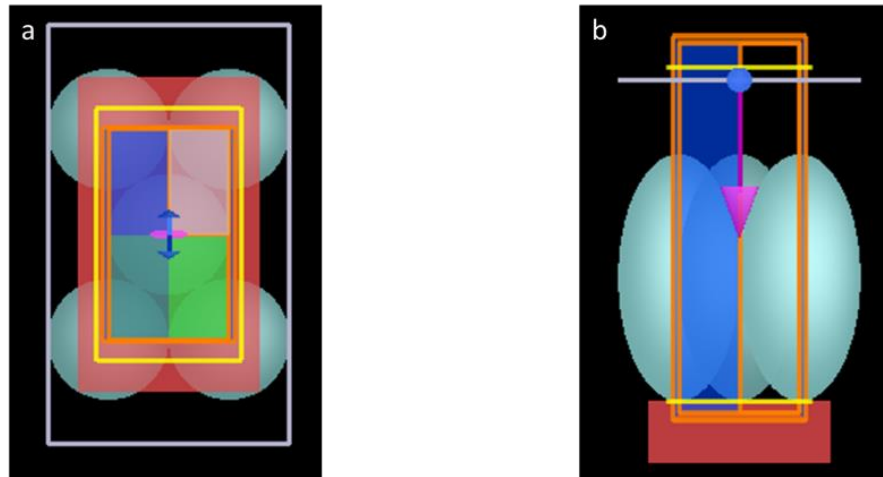

Figure B.1: Configuration of spherical design of glass on silicon in Lumerical, (a) top view and (b) side view.
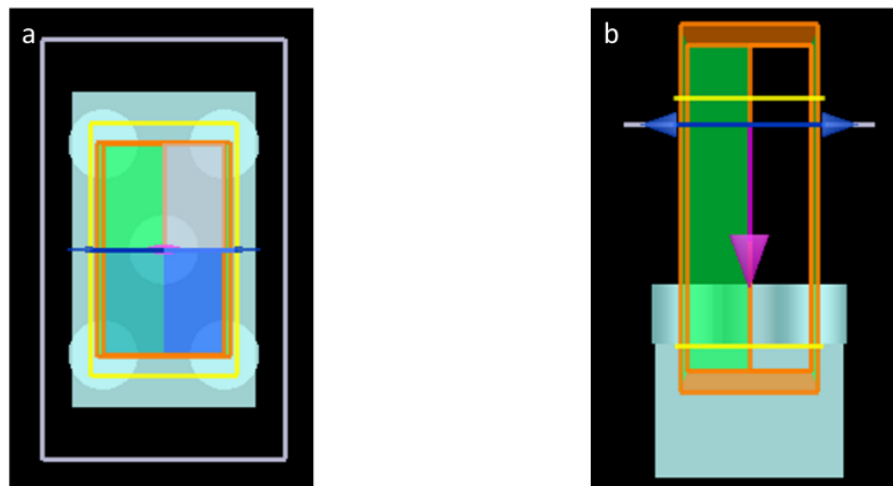

Figure B.2: Configuration of cylindrical design in Lumerical, (a) top view and (b) side view.

C. APPENDIX: Convergence tests

For both our designs, FDTD simulations are used to optimize the PRC effect. The mesh and minimal auto-shutoff convergence for the silica spheres on top of silicon and for the silica cylinders etched into is shown in Figure C.1 and Figure C.2, respectively. From the figures, it can be seen that for the spherical geometry, a mesh of 100 nm is enough, and a minimal auto-shutoff of 1e-4. While, for the cylindrical geometry, a mesh is needed of 50 nm and a minimal auto-shutoff of 1e-7. This difference in auto-shutoff implicates that higher Q modes are excited in the cylindrical geometry.
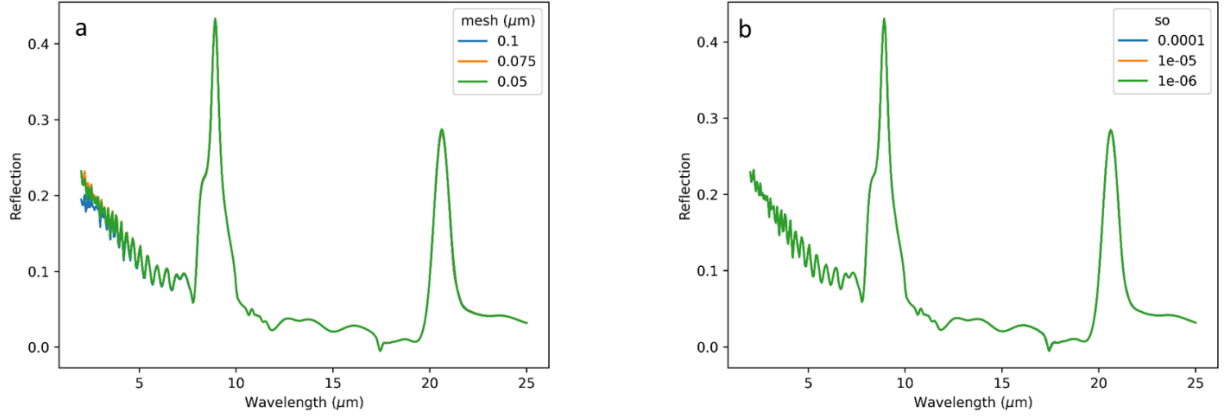

Figure C.1: Convergence tests of the spherical configuration of SiO_2, (a) the mesh convergence and (b) the minimal auto-shutoff convergence.
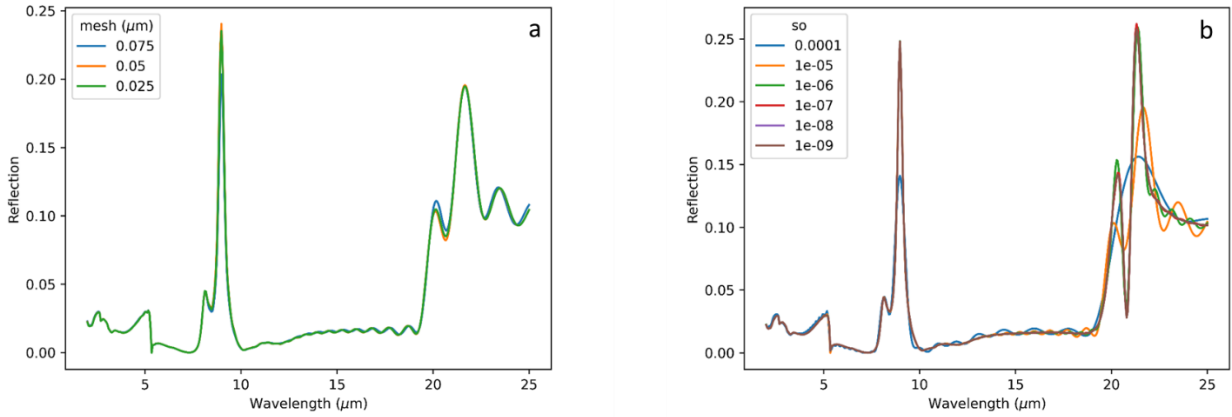

Figure C.2: Convergence test of cylindrical geometry of SiO_2, (a) the mesh convergence and (b) the minimal auto-shutoff convergence.

D. APPENDIX: Variance in SEM images

In Figure D.1 the SEM images are shown of a crosscut from the etched cylinders into the silica at two different positions. Firstly, the diameter varies between 3.65 and 3.87 µm, which is already larger than the 3.5 µm where we aimed for. The height is slightly smaller than what we aimed for and varies between 1.80 and 2.20 µm. Furthermore, from the images, a slight tilt is visible in the sides of the cylinders, which will influence the reflectance. However, cones are shown to work well for anti-reflection, so we expect this will only increase the emissivity slightly.
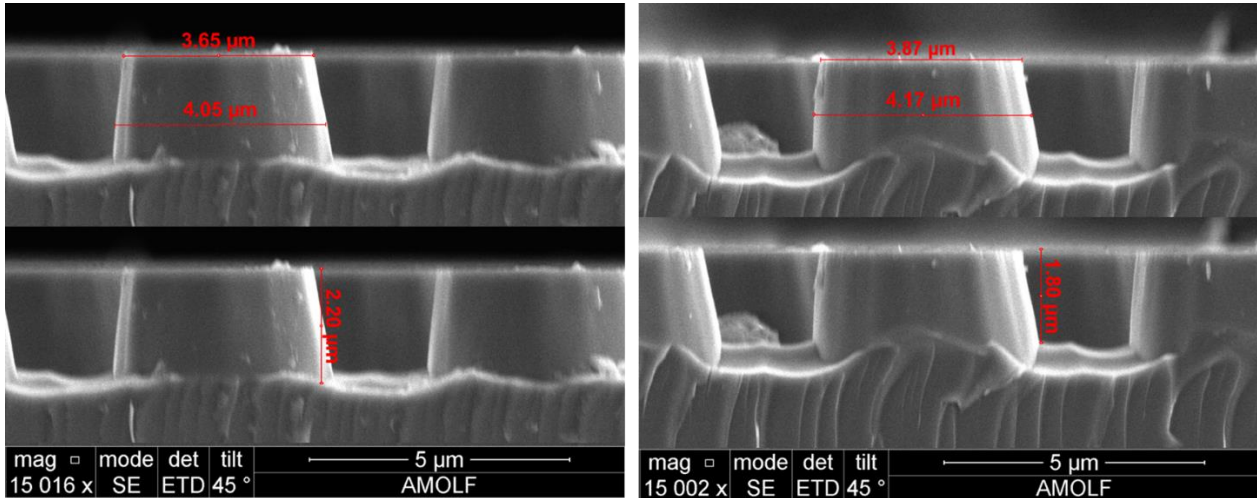

Figure D.1: SEM images of the cylinders etched in silica, on different places on the cross-section.

E. APPENDIX: Extended FTIR setup

Figure E.1 and Figure E.2 show a front image of the FTIR setup extended with the integrating sphere on the right and a top view of the path the infrared light travels through the system, respectively.
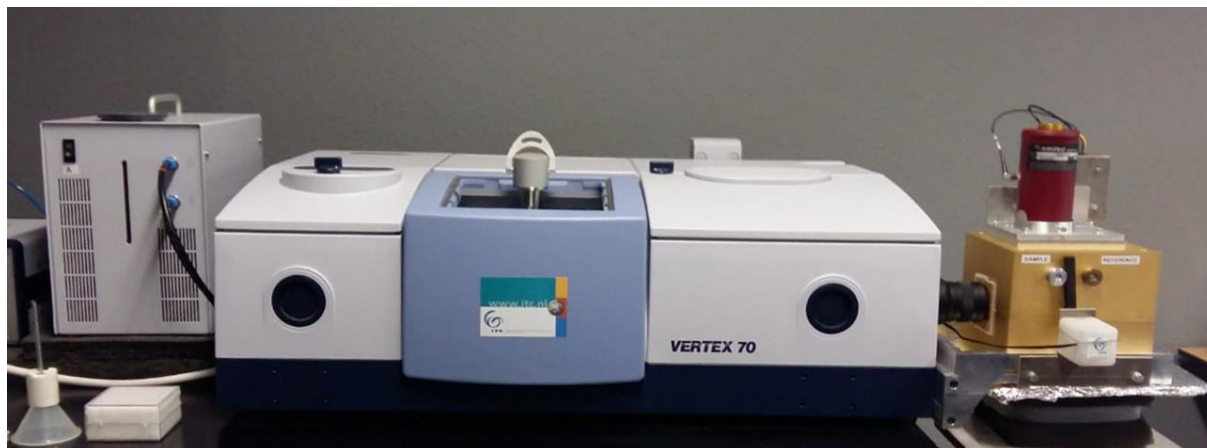

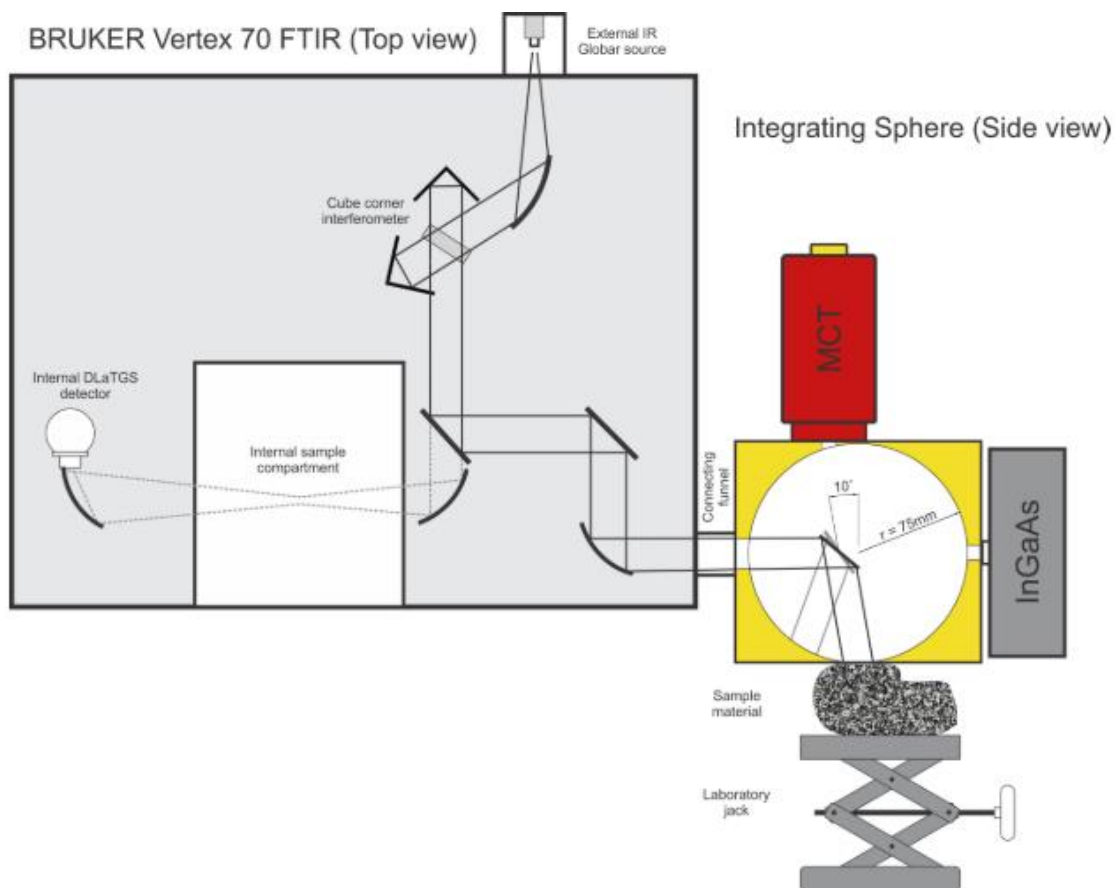*Figure E.1: Picture of the FTIR setup with an external integrating sphere.*

Figure E.2: Schematic representation of the path of the light used to measure the hemispherical reflectance with the FTIR setup.[56]

Bibliograpy

1   W. Shockley and H. J. Queisser, *J. Appl. Phys.*, 1961, **32**, 510–519.

2   A. Richter, M. Hermle and S. W. Glunz, *IEEE J. Photovoltaics*, 2013, **3**, 1184–1191.

3   K. Yoshikawa, H. Kawasaki, W. Yoshida, T. Irie, K. Konishi, K. Nakano, T. Uto, D. Adachi, M. Kanematsu, H. Uzu and K. Yamamoto, *Nat. Energy*, 2017, **2**, 17032.

4   E. Skoplaki and J. A. Palyvos, *Sol. Energy*, 2009, **83**, 614–624.

5   D. H. Otth and R. G. Ross, *Proceedings, Annu. Tech. Meet. - Inst. Environ. Sci.*, 1983, 121–126.

6   D. Beysens, I. Milimouk, V. Nikolayev, M. Muselli and J. Marcillat, *J. Hydrol.*, 2003, **276**, 1–11.

7   D. Zhao, X. Yin, J. Xu, G. Tan and R. Yang, *Energy*, 2020, **190**, 116322.

8   A. P. Raman, M. A. Anoma, L. Zhu, E. Rephaeli and S. Fan, *Nature*, 2014, **515**, 540–544.

9   W. Li, Y. Shi, K. Chen, L. Zhu and S. Fan, *ACS Photonics*, 2017, **4**, 774–782.

10   M. Zahir and M. Benlattar, *Appl. Opt.*, 2021, **60**, 445.

11   G. Perrakis, A. C. Tasolamprou, G. Kenanakis, E. N. Economou, S. Tzortzakis and M. Kafesaki, *Sci. Rep.*, 2021, **11**, 1–10.

12   J. Jaramillo-Fernandez, G. L. Whitworth, J. A. Pariente, A. Blanco, P. D. Garcia, C. Lopez and C. M. Sotomayor-Torres, *Small*, 2019, **15**, 1–9.

13   L. Long, Y. Yang and L. Wang, *Sol. Energy Mater. Sol. Cells*, 2019, **197**, 19–24.

14   E. Lee and T. Luo, *Sol. Energy Mater. Sol. Cells*, 2019, **194**, 222–228.

15   L. Zhu, A. P. Raman and S. Fan, *Proc. Natl. Acad. Sci. U. S. A.*, 2015, **112**, 12282–12287.

16   L. Zhu, A. Raman, K. X. Wang, M. A. Anoma and S. Fan, *Optica*, 2014, **1**, 32.

17   M. Gao, Y. Xia, R. Li, Z. Zhang, Y. He, C. Zhang, L. Chen, L. Qi, Y. Si, Q. Zhang and Y. Zheng, *Nanomaterials*, 2020, **10**, 1–11.

18   B. Zhao, M. Hu, X. Ao, Q. Xuan and G. Pei, *Sol. Energy Mater. Sol. Cells*, 2018, **178**, 266–272.

19   Q. Zhai and Q. Zhu, *Sol. Energy Mater. Sol. Cells*, 2021, **228**, 111117.

20   G. Chen, Y. Wang, J. Qiu, J. Cao, Y. Zou, S. Wang, J. Ouyang, D. Jia and Y. Zhou, *J. Mater. Sci. Technol.*, 2021, **90**, 76–84.

21   C. Ziming, W. Fuqiang, G. Dayang, L. Huaxu and S. Yong, *Sol. Energy Mater. Sol. Cells*, 2020, **213**, 110563.

22   T. A. S. for T. and Materials, Reference Air Mass 1.5 Spectra, https://www.nrel.gov/grid/solar-resource/spectra-am1.5.html.

23   E. Hecht, *Optics, 4e*, Pearson Education Limited, 2013.

24   Gemini Observatory, https://webarchive.gemini.edu/20210512-sciops--instruments--michelle/mid-ir-atmospheric-transmission.html.

25   J. Stefan, *Vienna, Sitzungsberichte der Math. Cl. der Kais. Akad. der Wissenschaften*, 1879, 79, 391–428.

26   S. J. Byrnes, 2016, 1–20.

27   T. H. Fung, T. Veeken, D. Payne, B. Veettil, A. Polman and M. Abbott, *Opt. Express*, 2019, **27**, 38645.

28   T. J. Bright, J. I. Watjen, Z. M. Zhang, C. Muratore and A. A. Voevodin, *Thin Solid Films*, 2012, **520**, 6793–6802.

29   V. A. Markel, *J. Opt. Soc. Am. A*, 2016, **33**, 1244.

30   C. F. Bohren and D. R. Huffman, *Absorption and scattering of light by small particles*, John Wiley & Sons, Ltd, Wiley Prof., 1983.

31   J. van de Groep and A. Polman, *Opt. Express*, 2013, **21**, 26285.

32   I. Staude, A. E. Miroshnichenko, M. Decker, N. T. Fofang, S. Liu, E. Gonzales, J. Dominguez, T. S. Luk, D. N. Neshev, I. Brener and Y. Kivshar, *ACS Nano*, 2013, **7**, 7824–7832.

33   R. Alaee, R. Filter, D. Lehr, F. Lederer and C. Rockstuhl, *Opt. Lett.*, 2015, **40**, 2645.

34   E. D. Palik, *Handbook of optical constants of solids*, Academic press, 1998, vol. 3.

35   J. Luo, N. J. Smith, C. G. Pantano and S. H. Kim, *J. Non. Cryst. Solids*, 2018, **494**, 94–103.

36   M. Rubin, *Sol. Energy Mater.*, 1985, **12**, 275–288.

37   J. Kischkat, S. Peters, B. Gruska, M. Semtsiv, M. Chashnikova, M. Klinkmüller, O. Fedosenko, S. Machulik, A. Aleksandrova, G. Monastyrskyi, Y. Flores and W. T. Masselink, *Appl. Opt.*, 2012, **51**, 6789–6798.

38   T. Siefke, S. Kroker, K. Pfeiffer, O. Puffky, K. Dietrich, D. Franta, I. Ohlídal, A. Szeghalmi, E. B. Kley and A. Tünnermann, *Adv. Opt. Mater.*, 2016, **4**, 1780–1786.

39   T. Mito, S. Fujino, H. Takebe, K. Morinaga, S. I. Todoroki and S. Sakaguchi, *J. Non. Cryst. Solids*, 1997, **210**, 155–162.

40   H. D. Omar, M. R. Hashim and M. Z. Pakhuruddin, *Optik (Stuttg).*, 2020, **219**, 165279.

41   P. Spinelli, M. A. Verschuuren and A. Polman, *Nat. Commun.*, 2012, **3**, 1–5.

42   Z. Y. Wang, R. J. Zhang, S. Y. Wang, M. Lu, X. Chen, Y. X. Zheng, L. Y. Chen, Z. Ye and C. Z. Wang, 2015, 1–6.

43   Y. Wang, L. Chen, H. Yang, Q. Guo, W. Zhou and M. Tao, *Mater. Sci. Pol.*, 2010, **28**, 467–478.

44   K. N. Al-Milaji, R. R. Secondo, T. N. Ng, N. Kinsey and H. Zhao, *Adv. Mater. Interfaces*, , DOI:10.1002/admi.201701561.

45   P. Kumnorkaew, Y. K. Ee, N. Tansu and J. F. Gilchrist, *Langmuir*, 2008, **24**, 12150–12157.

46   Lumerical Inc., https://www.lumerical.com/products/.

47   G. Kirchhoff, *London, Edinburgh, Dublin Philos. Mag. J. Sci.*, 1860, **20**, 1–21.

48   A. B. Evlyukhin, T. Fischer, C. Reinhardt and B. N. Chichkov, *Phys. Rev. B*, 2016, **94**, 1–7.

49   A. B. Evlyukhin, C. Reinhardt, E. Evlyukhin and B. N. Chichkov, *J. Opt. Soc. Am. B*, 2013, **30**, 2589.

50   A. S. Dimitrov and K. Nagayama, *Langmuir*, 1996, **12**, 1303–1311.

51   K. Sefiane, L. Tadrist and M. Douglas, *Int. J. Heat Mass Transf.*, 2003, **46**, 4527–4534.

52   R. D. Deegan, O. Bakajin, T. F. Dupont, G. Huber, S. R. Nagel and T. A. Witten, *Nature*, 1997, **389**, 827–829.

53   H. Hu and R. G. Larson, *J. Phys. Chem. B*, 2006, **110**, 7090–7094.

54   R. Bhardwaj, X. Fang, P. Somasundaran and D. Attinger, *Langmuir*, 2010, **26**, 7833–7842.

55   J. R. Vig, *Proc. - Electrochem. Soc.*, 1990, **90**, 105–113.

56   C. Hecker, S. Hook, M. van der Meijde, W. Bakker, H. van Werff, H. Wilbrink, F. van Ruitenbeek, B. de Smeth and F. van der Meer, *Sensors*, 2011, **11**, 10981–10999.

57   S. H. Suthar, N. Chandwani and C. Jariwala, *IOP Conf. Ser. Mater. Sci. Eng.*, , DOI:10.1088/1757-899X/404/1/012031.

58   M. Steffanson and I. W. Rangelow, *Opto-electronics Rev.*, 2014, **22**, 1–15.

Acknowledgments

After 10 months of working on this project, I would like to acknowledge the people that supported me, without whom this thesis would not have been possible. First of all, I would like to thank Albert for giving me the opportunity to work on this project in such an inspiring and supportive environment as AMOLF. Your enthusiasm for science is contagious and it was a true honor to work with you. Also, I would also like to thank Jorik van de Groep, who agreed to be the second examiner on this project and whose expertise on resonant structures and Mie resonators pushed me to understand the physics behind our photonic structures.

Secondly, I would like to thank Tom Veeken, who was my daily supervisor during this project. Tom, thank you for the time and effort you put into helping me during this project. Your supervision was absolutely great, and I really enjoyed our discussions and brainstorming sessions about what to do next or how to solve a problem. I am really happy with what we achieved in this project and I hope you still have time to finish the last loose ends and bring it to a higher level.

The main results of this project would not have been possible without our collaborator from ITO in Twente, Chris Hecker. His heavily modified FTIR setup with external integrating sphere allowed us to measure the hemispherical reflectance and thus to be able to compare the optical properties of our structures with simulations. Thank you for allowing us to use your setup for our measurements.

Of course, within AMOLF there are a lot of other people who helped and supported me the past year. I would like to thank you Photonic Materials group for their input in the weekly group meetings and of course the cleanroom staff for helping me with the fabrication. Always when I saw something odd, or something just did not work, I only had to ask and they would help out.

Finally, I would like to thank the people outside of AMOLF for getting me through this winter. Working from home is not always fun and my roommates really brightened this time with house diners and Friday afternoon drinks. And, last but not least, my parents and brother, who always supported me and were always there to listen. Thank you!